

---

# Diffusion Models Learn Low-Dimensional Distributions via Subspace Clustering

---

Anonymous Author(s)

Affiliation

Address

email

## Abstract

1           Recent empirical studies have demonstrated that diffusion models can effectively  
2           learn the image distribution and generate new samples. Remarkably, these mod-  
3           els can achieve this even with a small number of training samples despite a large  
4           image dimension, circumventing the curse of dimensionality. In this work, we  
5           provide theoretical insights into this phenomenon by leveraging key empirical ob-  
6           servations: (i) the low intrinsic dimensionality of image data, (ii) a union of man-  
7           ifold structure of image data, and (iii) the low-rank property of the denoising au-  
8           toencoder in trained diffusion models. These observations motivate us to assume  
9           the underlying data distribution of image data as a mixture of low-rank Gaussians  
10          and to parameterize the denoising autoencoder as a low-rank model according to  
11          the score function of the assumed distribution. With these setups, we rigorously  
12          show that optimizing the training loss of diffusion models is equivalent to solving  
13          the canonical subspace clustering problem over the training samples. Based on  
14          this equivalence, we further show that the minimal number of samples required to  
15          learn the underlying distribution scales linearly with the intrinsic dimensions un-  
16          der the above data and model assumptions. This insight sheds light on why diffu-  
17          sion models can break the curse of dimensionality and exhibit the phase transition  
18          from failure to success in learning distributions. Moreover, we empirically estab-  
19          lish a correspondence between the subspaces and the semantic representations of  
20          image data, facilitating image editing. We validate these results with extensive  
21          experimental results on both simulated distributions and image datasets.

## 22 1 Introduction

23          Generative modeling is a fundamental task in deep learning, which aims to learn a data distribution  
24          from training data to generate new samples. Recently, diffusion models have emerged as a new fam-  
25          ily of generative models, demonstrating remarkable performance across diverse domains, including  
26          image generation [1, 2, 3], video content generation [4, 5], speech and audio synthesis [6, 7], and  
27          solving inverse problem [8, 9]. In general, diffusion models learn a data distribution from train-  
28          ing samples through a process that imitates the non-equilibrium thermodynamic diffusion process  
29          [2, 10, 11]. Specifically, the training and sampling of diffusion models involve two stages: (i) a  
30          forward diffusion process where Gaussian noise is incrementally added to training samples at each  
31          time step, and (ii) a backward sampling process where the noise is progressively removed through  
32          a neural network that is trained to approximate the score function at all time steps. As described in  
33          prior works [12, 11], the generative capability of diffusion models lies in their ability to learn the  
34          *score function* of the data distribution, i.e., the gradient of the logarithm of the *probability density*  
35          *function (pdf)*. We refer the reader to [13, 14, 15] for a more comprehensive introduction and survey  
36          on diffusion models.

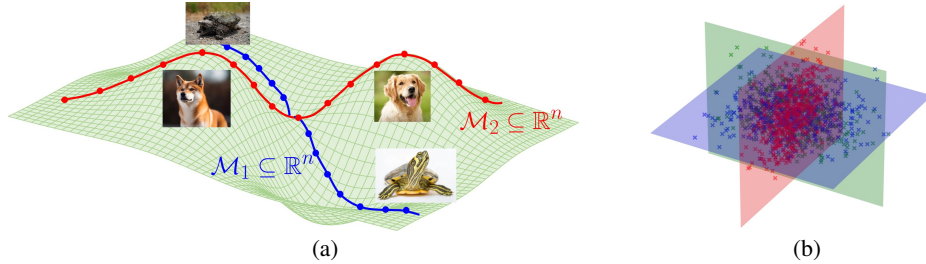


Figure 1: (a) Visualization of the union of manifold structure of image data. Here, different images lie on different manifolds  $\mathcal{M}_i \subseteq \mathbb{R}^n$  of intrinsic dimension  $d$  with  $d \ll n$ . (b) An illustration of training samples that are generated according to the MoLRG model. This model is a local linearization of a union of manifolds.

37 Despite the recent advances in understanding sampling convergence [16, 17, 18], distribution learn-  
 38 ing [19, 20], memorization [21, 22, 23, 24], and generalization [25, 26, 27] of diffusion models, the  
 39 fundamental working mechanisms remain poorly understood. One of the key questions is

40 *When and why can diffusion models learn the underlying data distribution without suffering from*  
 41 *the curse of dimensionality?*

42 At first glance, the answer might seem quite straightforward. If a diffusion model can learn the empir-  
 43 ical distribution of the training data that accurately approximates the underlying data distribution,  
 44 then the puzzle is solved! However, it has been shown in [28] that the number of samples for an  
 45 empirical distribution to approximate the underlying data distribution could grow exponentially with  
 46 respect to (*w.r.t.*) the data dimension. Moreover, [20, 29] showed that to learn an  $\epsilon$ -accurate score  
 47 estimator measured by the  $\ell_2$ -norm via score matching or kernel-based approach, the required size  
 48 of training samples grows at the rate of  $O(\epsilon^{-n})$ , where  $n$  is the data dimension. These theoretical  
 49 findings indicate that learning the underlying distribution via diffusion models suffers from the curse  
 50 of dimensionality. In contrast, recent studies [25, 27] showed that the number of training samples  
 51 for a diffusion model to learn the underlying distribution is much *smaller* than the worst-case sce-  
 52 nario, breaking the curse of dimensionality. Therefore, there is a significant gap between theory and  
 53 practice.

54 In this work, we aim to address the above question of learning the underlying distribution via dif-  
 55 fusion models by leveraging low-dimensional models. Our key observations are as follows: (i) The  
 56 intrinsic dimensionality of real image data is significantly lower than the ambient dimension, a fact  
 57 well-supported by extensive empirical evidence in [30, 31, 32]; (ii) Image data lies on a disjoint  
 58 union of manifolds of varying intrinsic dimensions, as empirically verified in [33, 34, 35] (see Fig-  
 59 ure 1(a)); (iii) We empirically observe that the denoising autoencoder (DAE) [36, 37] of diffusion  
 60 models trained on real-world image datasets exhibit low-rank structures (see Figure 2). Based on  
 61 these observations, we conduct a theoretical investigation of distribution learning through diffusion  
 62 models by assuming that (i) the underlying data distribution is a *mixture of low-rank Gaussians* (see  
 63 Definition 1) and (ii) the denoising autoencoder is parameterized according to the score function of  
 64 the MoLRG. Notably, these assumptions will be carefully discussed based on the existing literature  
 65 and validated by our experiments on real image datasets.

## 66 1.1 Our Contributions

67 This work studies the DAE-based training loss of diffusion models under the above low-dimensional  
 68 data model and network parameterization. Our contributions can be summarized as follows:

- 69 • **Equivalence between training diffusion models and subspace clustering.** Under the above  
 70 setup, we show that the training loss of diffusion models is equivalent to the *unsupervised* subspace  
 71 clustering problem [38, 39, 40] (see Theorem 3). This equivalence implies that training diffusion  
 72 models is essentially learning low-dimensional manifolds of the data distribution.
- 73 • **Understanding breaking the curse of dimensionality in learning distributions.** By leveraging  
 74 the above equivalence and the data model, we show that if the number of samples exceed the  
 75 intrinsic dimension of the subspaces, the optimal solutions of the training loss can recover the  
 76 underlying distribution. This explains why diffusion models can break the curse of dimensionality.  
 77 Conversely, if the number of samples is insufficient, it may learn an incorrect distribution.

78 • **Correspondence between semantic representations and the subspaces.** Interestingly, we find  
 79 that the discovered low-dimensional subspaces in a pre-trained diffusion model possess *semantic*  
 80 meanings for natural images; see Figure 5. This motivates us to propose a training-free method to  
 81 edit images on a frozen-trained diffusion model.

## 82 2 Problem Setup

83 In this work, we consider an image dataset consisting of samples  $\{\mathbf{x}^{(i)}\}_{i=1}^N \subseteq \mathbb{R}^n$ , where each data  
 84 point is *i.i.d.* sampled from an underlying data distribution  $p_{\text{data}}(\mathbf{x})$ . Instead of learning this pdf  
 85 directly, score-based diffusion models aim to learn the score function from the training samples.

### 86 2.1 Preliminaries on Score-Based Diffusion Models

87 **Forward and reverse SDEs of diffusion models.** In general, diffusion models consist of forward  
 88 and reverse processes indexed by a continuous time variable  $t \in [0, 1]$ . Specifically, the forward  
 89 process progressively injects noise into the data. This process can be described by the following  
 90 stochastic differential equation (SDE):

$$d\mathbf{x}_t = f(t)\mathbf{x}_t dt + g(t)d\mathbf{w}_t, \quad (1)$$

91 where  $\mathbf{x}_0 \sim p_{\text{data}}$ , the scalar functions  $f(t), g(t) : \mathbb{R} \rightarrow \mathbb{R}$  respectively denote the drift and diffusion  
 92 coefficients,<sup>1</sup> and  $\{\mathbf{w}_t\}_{t \in [0,1]}$  is the standard Wiener process. For ease of exposition, let  $p_t(\mathbf{x})$  denote  
 93 the pdf of  $\mathbf{x}_t$  and  $p_t(\mathbf{x}_t|\mathbf{x}_0)$  the transition kernel from  $\mathbf{x}_0$  to  $\mathbf{x}_t$ . According to Eq. (1), we have

$$p_t(\mathbf{x}_t|\mathbf{x}_0) = \mathcal{N}(\mathbf{x}_t; s_t\mathbf{x}_0, s_t^2\sigma_t^2\mathbf{I}_n), \text{ where } s_t = \exp\left(\int_0^t f(\xi)d\xi\right), \sigma_t = \sqrt{\int_0^t \frac{g^2(\xi)}{s^2(\xi)}d\xi}, \quad (2)$$

94 where  $s_t := s(t)$  and  $\sigma_t := \sigma(t)$  for simplicity. The reverse process gradually removes the noise  
 95 from  $\mathbf{x}_1$  via the following reverse-time SDE:

$$d\mathbf{x}_t = (f(t)\mathbf{x}_t - g^2(t)\nabla \log p_t(\mathbf{x}_t)) dt + g(t)d\bar{\mathbf{w}}_t, \quad (3)$$

96 where  $\{\bar{\mathbf{w}}_t\}_{t \in [0,1]}$  is another standard Wiener process, independent of  $\{\mathbf{w}_t\}$ , running backward in  
 97 time from  $t = 1$  to  $t = 0$ . It is worth noting that if  $\mathbf{x}_1$  and  $\nabla \log p_t$  are provided, the reverse process  
 98 has exactly the same distribution as the forward process at each time  $t \geq 0$  [42].

99 **Training loss of diffusion models.** Unfortunately, the score function  $\nabla \log p_t$  is usually unknown,  
 100 as it depends on the underlying data distribution  $p_{\text{data}}$ . To enable data generation via the reverse  
 101 SDE (3), a common approach is to estimate the score function  $\nabla \log p_t$  using the training samples  
 102  $\{\mathbf{x}^{(i)}\}_{i=1}^N$  based on the scoring matching [2, 11]. Because of the equivalence between the score  
 103 function  $\nabla \log p_t(\mathbf{x}_t)$  and the posterior mean  $\mathbb{E}[\mathbf{x}_0|\mathbf{x}_t]$ , i.e.,

$$s_t\mathbb{E}[\mathbf{x}_0|\mathbf{x}_t] = \mathbf{x}_t + s_t^2\sigma_t^2\nabla \log p_t(\mathbf{x}_t), \quad (4)$$

104 according to Tweedie’s formula and (2), an alternative approach to estimate the score function  
 105  $\nabla \log p_t$  is to estimate the posterior mean  $\mathbb{E}[\mathbf{x}_0|\mathbf{x}_t]$ . Consequently, extensive works [43, 25, 41,  
 106 37, 44] have considered training a time-dependent function  $\mathbf{x}_\theta(\cdot, t) : \mathbb{R}^n \times [0, 1] \rightarrow \mathbb{R}^n$ , known as  
 107 *denoising autoencoder* (DAE), parameterized by a neural network with parameters  $\theta$  to estimate the  
 108 posterior mean  $\mathbb{E}[\mathbf{x}_0|\mathbf{x}_t]$ . To determine the parameters  $\theta$ , we can minimize the following empirical  
 109 loss:

$$\min_{\theta} \ell(\theta) := \frac{1}{N} \sum_{i=1}^N \int_0^1 \lambda_t \mathbb{E}_{\epsilon \sim \mathcal{N}(0, \mathbf{I}_n)} \left[ \left\| \mathbf{x}_\theta(s_t\mathbf{x}^{(i)} + \gamma_t\epsilon, t) - \mathbf{x}^{(i)} \right\|^2 \right] dt, \quad (5)$$

110 where  $\lambda_t : [0, 1] \rightarrow \mathbb{R}^+$  is a weighting function and  $\gamma_t := s_t\sigma_t$ . As shown in [37], training the DAE  
 111 is equivalent to performing explicit or implicit score matching under mild conditions. We refer the  
 112 reader to Appendix A.1 for the relationship between this loss and the score-matching loss.

<sup>1</sup>In general, the functions  $f(t)$  and  $g(t)$  are chosen such that (i)  $\mathbf{x}_t$  for all  $t$  close to 0 approximately follows the data distribution  $p_{\text{data}}$  and (ii)  $\mathbf{x}_t$  for all  $t$  close to 1 is nearly a standard Gaussian distribution; see, e.g., the settings in [2, 41, 11].

113 **2.2 Low-Dimensional Data and Models**

114 **Mixture of low-rank Gaussian data distribution.** Although real-world image datasets are  
 115 high dimensional in terms of pixel count and overall data volume, extensive empirical works  
 116 [30, 34, 31, 32] suggest that their intrinsic dimensions are much lower. For instance, [31] indicated  
 117 that even for complex datasets like ImageNet [45], the intrinsic dimensionality is approximately 40,  
 118 which is significantly lower than its ambient dimension. Recently, [33, 34, 35] empirically validated  
 119 the *union of manifolds* hypothesis, demonstrating that high-dimensional image data often lies on a  
 120 disjoint union of manifolds instead of a single manifold. These observations motivate us to model  
 121 the underlying data distribution as a *mixture of low-rank Gaussians*, where the data points are gen-  
 122 erated from a mixture of several Gaussian distributions; see Figure 1(b). We formally define the  
 123 MoLRG distribution as follows:

124 **Definition 1** (Mixtures of Low-Rank Gaussians). *We say that a random vector  $\mathbf{x} \in \mathbb{R}^n$  follows a*  
 125 *mixture of  $K$  low-rank Gaussian distribution with parameters  $\{\pi_k\}_{k=1}^K$  and  $\{\mathbf{U}_k^*\}_{k=1}^K$  if*

$$\mathbf{x} \sim \sum_{k=1}^K \pi_k \mathcal{N}(\mathbf{0}, \mathbf{U}_k^* \mathbf{U}_k^{*T}), \quad (6)$$

126 where  $\mathbf{U}_k^* \in \mathcal{O}^{n \times d_k}$  denotes the orthonormal base of the  $k$ -th component and  $\pi_k \geq 0$  is the mixing  
 127 proportion of the  $k$ -th mixture component satisfying  $\sum_{k=1}^K \pi_k = 1$ .

128 Before we proceed, we make some remarks on this data model. First, to study how diffusion mod-  
 129 els learn the underlying data distribution, many recent works have studied a mixture of full-rank  
 130 Gaussian distributions (see Eq. (20)); see, e.g., [46, 47, 48]. However, compared to this model,  
 131 MoLRG is a more suitable model for capturing the low-dimensionality in image data distribution.  
 132 Second, [33, 34] conducted extensive numerical experiments to validate that image datasets such  
 133 as MNIST and ImageNet approximately lie on a union of low-dimensional manifolds. Because a  
 134 nonlinear manifold can be well approximated by its tangent space (i.e., a linear subspace) in a local  
 135 neighborhood, the MoLRG model, which represents data as a union of linear subspace, serves a good  
 136 local approximation of a union of manifolds. Finally, assuming Gaussian distributions in each sub-  
 137 space in the MoLRG model is to ensure theoretical tractability, making it a practical starting point for  
 138 theoretical studies on real-world image datasets. Now, we compute the ground-truth posterior mean  
 139  $\mathbb{E}[\mathbf{x}_0 | \mathbf{x}_t]$  when  $\mathbf{x}_0$  satisfies the MoLRG model as follows.

140 **Lemma 1.** *Suppose that  $\mathbf{x}_0$  satisfies the MoLRG model. For each time  $t > 0$ , it holds that*

$$\mathbb{E}[\mathbf{x}_0 | \mathbf{x}_t] = \frac{s_t}{s_t^2 + \gamma_t^2} \frac{\sum_{k=1}^K \pi_k \exp(\phi_t \|\mathbf{U}_k^{*T} \mathbf{x}_t\|^2) \mathbf{U}_k^* \mathbf{U}_k^{*T} \mathbf{x}_t}{\sum_{k=1}^K \pi_k \exp(\phi_t \|\mathbf{U}_k^{*T} \mathbf{x}_t\|^2)}, \text{ where } \phi_t := \frac{s_t^2}{2\gamma_t^2(s_t^2 + \gamma_t^2)}. \quad (7)$$

141 We defer the proof of this lemma to Appendix A.2. Notably, this lemma provides guidance on the  
 142 network parameterization of the DAE  $\mathbf{x}_\theta(\cdot, t)$  as discussed below.

143 **Low-rank network parameterization.** When we train diffusion models with the U-Net architec-  
 144 ture [49] on various image datasets, it is observed that the numerical rank of the Jacobian of the  
 145 DAE, i.e.,  $\nabla_{\mathbf{x}_t} \mathbf{x}_\theta(\mathbf{x}_t, t)$ , is substantially lower than the ambient dimension in most time steps; see  
 146 Figure 2(a). When training diffusion models with U-Net on the samples generated according to the  
 147 MoLRG model, the Jacobian of the DAE also exhibits a similar low-rank pattern; see Figure 2(b). The  
 148 above observations motivate us to consider a low-rank parameterization of the network. According  
 149 to the ground-truth posterior mean of the MoLRG model in Lemma 1, a natural parameterization for  
 150 the DAE is

$$\mathbf{x}_\theta(\mathbf{x}_t, t) = \frac{s_t}{s_t^2 + \gamma_t^2} \sum_{k=1}^K w_k(\boldsymbol{\theta}; \mathbf{x}_t) \mathbf{U}_k \mathbf{U}_k^T \mathbf{x}_t, \quad w_k(\boldsymbol{\theta}; \mathbf{x}_t) = \frac{\pi_k \exp(\phi_t \|\mathbf{U}_k^T \mathbf{x}_t\|^2)}{\sum_{l=1}^K \pi_l \exp(\phi_t \|\mathbf{U}_l^T \mathbf{x}_t\|^2)}, \quad (8)$$

151 where the network parameters  $\boldsymbol{\theta} = \{\mathbf{U}_k\}_{k=1}^K$  satisfy  $\mathbf{U}_k \in \mathcal{O}^{n \times d_k}$ . Although this approach may  
 152 seem idealized, it offers several practical insights. First, if we consider a single low-rank Gaussian,  
 153 the network parameterization takes the form  $\mathbf{x} - s_t / (s_t^2 + \gamma_t^2) \mathbf{U} \mathbf{U}^T \mathbf{x}$ , which resembles the structure  
 154 of a practical U-Net with a linear encoder, decoder, and skip connections. This provides theoretical  
 155 insights into why U-Net is preferred for training diffusion models. Second, to learn the underlying  
 156 distribution, the number of samples should be proportional to its intrinsic dimension. In practice,

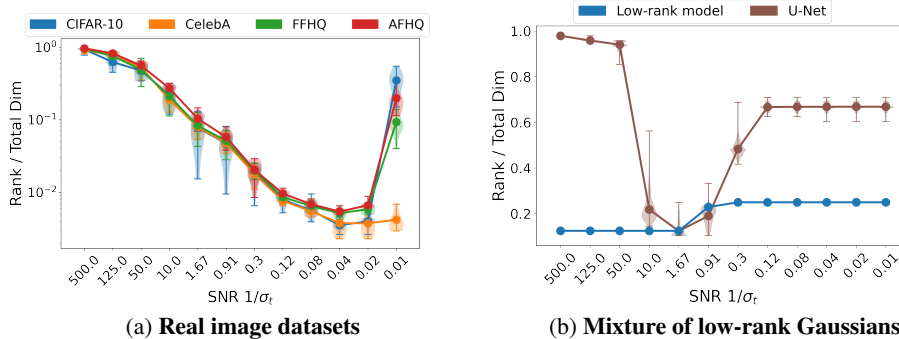


Figure 2: **Low-rank property of the DAE of trained diffusion models.** We plot the ratio of the numerical rank of the Jacobian of the denoising autoencoder, i.e.,  $\nabla_{\mathbf{x}_t} \mathbf{x}_\theta(\mathbf{x}_t, t)$ , over the total dimension against the signal-to-noise ratio (SNR)  $1/\sigma_t$  on trained diffusion models. (a) We train diffusion models on image datasets CIFAR-10, CelebA, FFHQ, and AFHQ. The experimental details are provided in Appendix C.1. (b) We respectively train diffusion models with the low-rank parameterization (8) and U-Net on a mixture of low-rank Gaussian distributions.

157 this informs us on how to use a minimal number of samples to train diffusion models to achieve  
 158 generalization.

159 Similar simplifications have been widely used for theoretical analysis in various ideal data distribu-  
 160 tions; see, e.g., [19, 46, 47, 48]. Notably, under this specific network parameterization in Eq. (8),  
 161 learning the score function  $\nabla \log p_t(\mathbf{x}_t)$  reduces to learning the network parameters  $\theta$  in Eq. (8)  
 162 according to Lemma 1 and Eq. (4).

### 163 3 Main Results

164 Based on the setups in Section 2.2, we are ready to conduct a theoretical analysis of distribution  
 165 learning using diffusion models.

#### 166 3.1 A Warm-Up Study: A Single Low-rank Gaussian Case

167 To begin, we start from a simple case that the underlying distribution  $p_{\text{data}}$  is a *single* low-rank  
 168 Gaussian. Specifically, the training samples  $\{\mathbf{x}^{(i)}\}_{i=1}^N \subseteq \mathbb{R}^n$  are generated according to

$$\mathbf{x}^{(i)} = \mathbf{U}^* \mathbf{a}_i + \mathbf{e}_i, \quad (9)$$

169 where  $\mathbf{U}^* \in \mathcal{O}^{n \times d}$  denotes an orthonormal basis,  $\mathbf{a}_i \stackrel{i.i.d.}{\sim} \mathcal{N}(\mathbf{0}, \mathbf{I}_d)$  is coefficients for each  $i \in [N]$ ,  
 170 and  $\mathbf{e}_i \in \mathbb{R}^n$  is noise for all  $i \in [N]$ .<sup>2</sup> According to (8), we parameterize the DAE into

$$\mathbf{x}_\theta(\mathbf{x}_t, t) = \frac{s_t}{s_t^2 + \gamma_t^2} \mathbf{U} \mathbf{U}^T \mathbf{x}_t, \quad (10)$$

171 where  $\theta = \mathbf{U} \in \mathcal{O}^{n \times d}$ . Equipped with the above setup, we can show the following result.

172 **Theorem 1.** *Suppose that the DAE  $\mathbf{x}_\theta(\cdot, t)$  in Problem (5) is parameterized into (10) for each*  
 173  *$t \in [0, 1]$ . Then, Problem (5) is equivalent to the following PCA problem:*

$$\max_{\mathbf{U} \in \mathbb{R}^{n \times d}} \sum_{i=1}^N \|\mathbf{U}^T \mathbf{x}^{(i)}\|^2 \quad \text{s.t.} \quad \mathbf{U}^T \mathbf{U} = \mathbf{I}_d. \quad (11)$$

174 We defer the proof to Appendix A.3. In the single low-rank Gaussian model, Theorem 1 shows  
 175 that training diffusion models with a DAE of the form (10) to learn this distribution is equivalent to  
 176 performing PCA on the training samples. Leveraging this equivalence, we can further characterize  
 177 the number of samples required for learning underlying distribution under the data model (9).

<sup>2</sup>Since real-world images inherently contain noise due to various factors, such as sensor limitation, environ-  
 ment conditions, and transition error, it is reasonable to add a noise term to this model.

178 **Theorem 2.** Consider the setting of Theorem 1. Suppose that the training samples  $\{\mathbf{x}^{(i)}\}_{i=1}^N$  are  
 179 generated according to the noisy single low-rank Gaussian model defined in (9). Let  $\hat{\mathbf{U}}$  denote an  
 180 optimal solution of Problem (5). The following statements hold:

181 i) If  $N \geq d$ , it holds with probability at least  $1 - 1/2^{N-d+1} - \exp(-c_2N)$  that any optimal solution  
 182  $\hat{\mathbf{U}}$  satisfies

$$\left\| \hat{\mathbf{U}}\hat{\mathbf{U}}^T - \mathbf{U}^*\mathbf{U}^{*T} \right\|_F \leq \frac{c_1 \sqrt{\sum_{i=1}^N \|\mathbf{e}_i\|^2}}{\sqrt{N} - \sqrt{d-1}}, \quad (12)$$

183 where  $c_1, c_2 > 0$  are constants that depend polynomially only on the Gaussian moment.

184 ii) If  $N < d$ , there exists an optimal solution  $\hat{\mathbf{U}} \in \mathcal{O}^{n \times d}$  such that with probability at least  $1 -$   
 185  $1/2^{d-N+1} - \exp(-c'_2d)$ ,

$$\left\| \hat{\mathbf{U}}\hat{\mathbf{U}}^T - \mathbf{U}^*\mathbf{U}^{*T} \right\|_F \geq \sqrt{2 \min\{d-N, n-d\}} - \frac{c'_1 \sqrt{\sum_{i=1}^N \|\mathbf{e}_i\|^2}}{\sqrt{d} - \sqrt{N-1}}, \quad (13)$$

186 where  $c'_1, c'_2 > 0$  are constants that depend polynomially only on the Gaussian moment.

187 **Remark 1.** We defer the proof to Appendix A.4. Building on the equivalence in Theorem 1 and the  
 188 DAE parameterization (10), Theorem 2 clearly shows a phase transition from failure to success in  
 189 learning the underlying distribution as the number of training samples increases. This phase transi-  
 190 tion is further corroborated by our experiments in Figures 3(a) and 3(b). Note that our theory cannot  
 191 explain why diffusion models memorize training data (i.e., learning the empirical distribution). This  
 192 is because the parameterization (10) is not as sufficiently over-parameterized as architectures like  
 193 U-Net. We plan to explore this over-parameterized setting in future work to better understand how  
 194 diffusion models achieve memorization and to extend our theoretical insights accordingly.

### 195 3.2 From Single Low-Rank Gaussian to Mixtures of Low-Rank Gaussians

196 In this subsection, we extend the above study to the MoLRG distribution. In particular, we consider  
 197 a noisy version of the MoLRG model as defined Definition 1. Specifically, the training samples are  
 198 generated by

$$\mathbf{x}^{(i)} = \mathbf{U}_k^* \mathbf{a}_i + \mathbf{e}_i \text{ with probability } \pi_k, \quad \forall i \in [N], \quad (14)$$

199 where  $\mathbf{U}_k^* \in \mathcal{O}^{n \times d_k}$  denotes an orthonormal basis for each  $k \in [K]$ ,  $\mathbf{a}_i \stackrel{i.i.d.}{\sim} \mathcal{N}(\mathbf{0}, \mathbf{I}_{d_k})$  is coeffi-  
 200 cients, and  $\mathbf{e}_i \in \mathbb{R}^n$  is noise for each  $i \in [N]$ . As argued by [33], image data lies on a *disjoint* union  
 201 of manifolds. This motivates us to assume that the basis matrices of subspaces satisfy  $\mathbf{U}_k^{*T} \mathbf{U}_l^* = \mathbf{0}$   
 202 for each  $k \neq l$ . To simplify our analysis, we assume that  $d_1 = \dots = d_K = d$  and the mixing  
 203 weights satisfy  $\pi_1 = \dots = \pi_K = 1/K$ . Moreover, we consider a hard-max counterpart of Eq. (8)  
 204 for the DAE parameterization as follows:

$$\mathbf{x}_\theta(\mathbf{x}_t, t) = \frac{s_t}{s_t^2 + \gamma_t^2} \sum_{k=1}^K \hat{w}_k(\boldsymbol{\theta}; \mathbf{x}_0) \mathbf{U}_k \mathbf{U}_k^T \mathbf{x}_t, \quad (15)$$

205 where  $\boldsymbol{\theta} = \{\mathbf{U}_k\}_{k=1}^K$  and the weights  $\{\hat{w}_k(\boldsymbol{\theta}; \mathbf{x}_0)\}_{k=1}^K$  are set as

$$\hat{w}_k(\boldsymbol{\theta}; \mathbf{x}_0) = 1, \text{ if } k = k_0, \hat{w}_k(\boldsymbol{\theta}; \mathbf{x}_0) = 0, \text{ otherwise,} \quad (16)$$

206 where  $k_0 \in [K]$  is an index satisfying  $\|\mathbf{U}_{k_0}^T \mathbf{x}_0\| \geq \|\mathbf{U}_l^T \mathbf{x}_0\|$  for all  $l \neq k_0 \in [K]$ . We should point  
 207 out that we use two key approximations here. First, the soft-max weights  $\{w_k(\boldsymbol{\theta}, \mathbf{x}_t)\}$  in Eq. (8)  
 208 are approximated by the hard-max weights  $\{\hat{w}_k(\boldsymbol{\theta}; \mathbf{x}_0)\}_{k=1}^K$ . Second,  $\|\mathbf{U}_k^T \mathbf{x}_t\|$  is approximated by  
 209 its expectation, i.e.,  $\mathbb{E}_\epsilon[\|\mathbf{U}_k^T \mathbf{x}_t\|^2] = \mathbb{E}_\epsilon[\|\mathbf{U}_k^T (s_t \mathbf{x}_0 + \gamma_t \boldsymbol{\epsilon})\|^2] = s_t^2 \|\mathbf{U}_k^T \mathbf{x}_0\|^2 + \gamma_t^2 d$ . We refer the  
 210 reader to Appendix B.1 for more details on these approximation. Now, we are ready to show the  
 211 following theorem.

212 **Theorem 3.** Suppose that the DAE  $\mathbf{x}_\theta(\cdot, t)$  in Problem (5) is parameterized into (15) for each  
 213  $t \in [0, 1]$ , where  $\hat{w}_k(\boldsymbol{\theta}, \mathbf{x}_0)$  is defined in (16) for each  $k \in [K]$ . Then, Problem (5) is equivalent to  
 214 the following subspace clustering problem:

$$\max_{\boldsymbol{\theta}} \frac{1}{N} \sum_{k=1}^K \sum_{i \in C_k(\boldsymbol{\theta})} \|\mathbf{U}_k^T \mathbf{x}^{(i)}\|^2 \quad \text{s.t.} \quad [\mathbf{U}_1, \dots, \mathbf{U}_K] \in \mathcal{O}^{n \times dK}, \quad (17)$$

215 where  $C_k(\boldsymbol{\theta}) := \{i \in [N] : \|\mathbf{U}_k^T \mathbf{x}^{(i)}\| \geq \|\mathbf{U}_l^T \mathbf{x}^{(i)}\|, \forall l \neq k\}$  for each  $k \in [K]$ .

216 We defer the proof to Appendix B.2. When the DAE is parameterized into (15), Theorem 3 demon-  
 217 strates that optimizing the training loss of diffusion models is equivalent to solving the subspace  
 218 clustering problem [39, 40]. Moreover, the equivalence allows us to characterize the required mini-  
 219 mum number of samples for learning the underlying MoLRG distribution.

220 **Theorem 4.** Consider the setting of Theorem 3. Suppose that the training samples  $\{\mathbf{x}^{(i)}\}_{i=1}^N$  are  
 221 generated by the MoLRG distribution in Definition 1. Suppose  $d \gtrsim \log N$  and  $\|\mathbf{e}_i\| \lesssim \sqrt{d/N}$  for  
 222 all  $i \in [N]$ . Let  $\{\hat{\mathbf{U}}_k\}_{k=1}^K$  denote an optimal solution of Problem (5) and  $N_k$  denote the number of  
 223 samples from the  $k$ -th Gaussian component. Then, the following statements hold:

224 (i) If  $N_k \geq d$  for each  $k \in [K]$ , there exists a permutation  $\Pi : [K] \rightarrow [K]$  such that with  
 225 probability at least  $1 - 2K^2N^{-1} - \sum_{k=1}^K (1/2^{N_k-d+1} + \exp(-c_2N_k))$  for each  $k \in [K]$ ,

$$\left\| \hat{\mathbf{U}}_{\Pi(k)} \hat{\mathbf{U}}_{\Pi(k)}^T - \mathbf{U}_k^* \mathbf{U}_k^{*T} \right\|_F \leq \frac{c_1 \sqrt{\sum_{i=1}^N \|\mathbf{e}_i\|^2}}{\sqrt{N_k} - \sqrt{d-1}}, \quad (18)$$

226 where  $c_1, c_2 > 0$  are constants that depend polynomially only on the Gaussian moment.

227 (ii) If  $N_k < d$  for some  $k \in [K]$ , there exists a permutation  $\Pi : [K] \rightarrow [K]$  and  $k \in [K]$  such  
 228 that with probability at least  $1 - 2K^2N^{-1} - \sum_{k=1}^K (1/2^{d-N_k+1} + \exp(-c'_2N_k))$ ,

$$\left\| \hat{\mathbf{U}}_{\Pi(k)} \hat{\mathbf{U}}_{\Pi(k)}^T - \mathbf{U}_k^* \mathbf{U}_k^{*T} \right\|_F \geq \sqrt{2 \min\{d - N_k, n - d\}} - \frac{c'_1 \sqrt{\sum_{i=1}^N \|\mathbf{e}_i\|^2}}{\sqrt{d} - \sqrt{N_k - 1}}, \quad (19)$$

229 where  $c'_1, c'_2 > 0$  are constants that depend polynomially only on the Gaussian

230 **Remark 2.** We defer the proof to Appendix B.3. We discuss the implications of our results below.

- 231 • *Phase transition in learning the underlying distribution.* This theorem demonstrates that when  
 232 the number of samples in each subspace exceeds the dimension of the subspace and the noise  
 233 is bounded, the optimal solution of the training loss (5) under the parameterization (15) can re-  
 234 cover the underlying subspaces up to the noise level. Conversely, when the number of samples is  
 235 insufficient, there exists an optimal solution that may recover wrong subspaces; see Figures 3(c,d).
- 236 • *Connections to the phase transition from memorization to generalization.* We should clarify the  
 237 difference between the phase transition described in Theorems 2 & 4 and the phase transition from  
 238 memorization to generalization. Our phase transition refers to the shift from failure to success of  
 239 learning the underlying distribution as the number of training samples increase, whereas the latter  
 240 concerns the shift from memorizing data to generalizing from it as the number of training samples  
 241 increases. Nevertheless, our theory still sheds light on the minimal number of samples required  
 242 for diffusion models to enter the generalized regime.

## 243 4 Experiments & Practical Implications

244 In this section, we first investigate phase transitions of diffusion models in learning distributions  
 245 under both theoretical and practical settings in Section 4.1. Next, we demonstrate the practical  
 246 implications of our work by exploring the correspondence between low-dimensional subspaces and  
 247 semantic representations for controllable image editing in Section 4.2.

### 248 4.1 Phase Transition in Learning Distributions

249 In this subsection, we conduct experiments on both synthetic and real datasets to study the phase  
 250 transition of diffusion models in learning distributions.

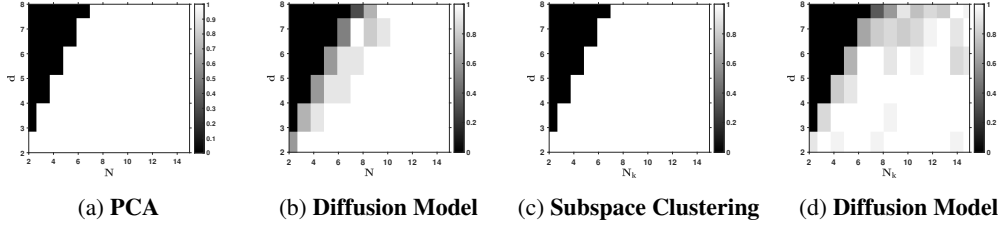


Figure 3: **Phase transition of learning the MoLRG distribution.** The  $x$ -axis is the number of training samples and  $y$ -axis is the dimension of subspaces. Darker pixels represent a lower empirical probability of success. When  $K = 1$ , we apply SVD and train diffusion models to solve Problems (11) and (5), visualizing the results in (a) and (b), respectively. When  $K = 2$ , we apply a subspace clustering method and train diffusion models for solving Problems (17) and (5), visualizing the results in (c) and (d), respectively.

251 **Learning the MoLRG distribution with the theoretical parameterizations.** To begin, we opti-  
 252 mize the training loss (5) with the theoretical parameterization (8), where the data samples are  
 253 generated by the MoLRG distribution. First, we apply stochastic gradient descent (see Algorithm 1)  
 254 to solve Problem (5) with the DAE parameterized as (8). For comparison, according to Theorem 1  
 255 (resp., Theorem 3), we apply a singular value decomposition (resp., subspace clustering [40]) to  
 256 solve Problem (11) (resp, Problem (17)). We conduct three sets of experiments, where the data  
 257 samples are respectively generated according to the single low-rank Gaussian distribution (9) with  
 258  $K = 1$  and a mixture of low-rank Gaussian distributions (14) with  $K = 2, 3$ . In each set, we set  
 259 the total dimension  $n = 48$  and let the subspace dimension  $d$  and the number of training samples  
 260  $N$  vary from 2 to 8 and 2 to 15 with increments of 1, respectively. For every pair of  $d$  and  $N$ , we  
 261 generate 20 instances, run the above methods, and calculate the successful rate of recovering the  
 262 underlying subspaces. The simulation results are visualized in Figure 3 and Figure 7. It is observed  
 263 that all these methods exhibit a phase transition from failure to success in learning the subspaces as  
 264 the number of training samples increases, which supports the results in Theorems 2 and 4.

265 **Learning the MoLRG distribution with U-Net.** Next, we optimize the training loss (5) with pa-  
 266 rameterizing the DAE  $x_\theta(\cdot, t)$  using U-Net, detailed experiment settings are in Appendix D.2. We  
 267 measure the generalization ability of U-Net via *generalization (GL) score* defined in Eq. (48). The  
 268 trained diffusion model is in the memorization regime when the GL score is close to 0, while it is  
 269 in the generalization regime when the GL score is close to 1. Detailed discussions about the metric  
 270 are in Appendix D.2. In the experiments, we generate the data samples using the MoLRG distribution  
 271 with  $K = 2$ ,  $n = 48$ , and  $d_k \in \{3, 4, 5, 6\}$ . Then, we plot the GL score against the  $N_k/d_k$  for  
 272 each  $d_k$  in Figure 4(a). It is observed that for a fixed  $d_k$ , the generalization performance of diffu-  
 273 sion models improves as the number of training samples increases. Notably, for different values of  
 274  $d_k$ , the plot of the GL score against the  $N_k/d_k$  remains approximately consistent. This observation  
 275 indicates that the phase transition curve for U-Net learning the MoLRG distribution depends on the  
 276 ratio  $N_k/d_k$  rather than on  $N_k$  and  $d_k$  individually. When  $N_k/d_k \approx 60$ , GL score  $\approx 1.0$  suggesting  
 277 that U-Net generalizes when  $N_k \geq 60d_k$ . This linear relationship for the phase transition differs  
 278 from  $N_k \geq d_k$  in Theorem 4 due to training with U-Net instead of the optimal network parame-  
 279 terization in Eq. (8). Nevertheless, Theorem 2 and Theorem 4 still provide valuable insights into  
 280 learning distributions via diffusion models by demonstrating a similar phase transition phenomenon  
 281 and confirming a linear relationship between  $N_k$  and  $d_k$ .

282 **Learning real image data distributions with U-Net.** Finally, we train diffusion models using U-  
 283 Net on real image datasets AFHQ, CelebA, FFHQ, and CIFAR-10. The detailed experiment settings  
 284 are deferred to Appendix D.3. we utilize the generalization (GL) score on the real-world image  
 285 dataset according to [27]. The definition of the metric is in Eq. (49) and detailed discussions are  
 286 in Appendix D.3. Intuitively, GL score measures the dissimilarity between the generated sample  
 287  $\mathbf{x}$  and all  $N$  samples  $\mathbf{y}_i$  from the training dataset  $\{\mathbf{y}_i\}_{i=1}^N$ . A higher GL score indicates stronger  
 288 generalizability. For each data set, we train U-Net and plot the GL score against the number of  
 289 training samples in Figure 4(b). The phase transition in the real dataset is illustrated in Figure 4(b).  
 290 As observed, the order in which the samples need to generalize follows the relationship: AFHQ  
 291  $>$  CelebA  $>$  FFHQ  $\approx$  CIFAR-10. Additionally, from our previous observations in Figure 2, the  
 292 relationship of the intrinsic dimensions for these datasets is: AFHQ  $>$  FFHQ  $>$  CelebA  $\approx$  CIFAR-

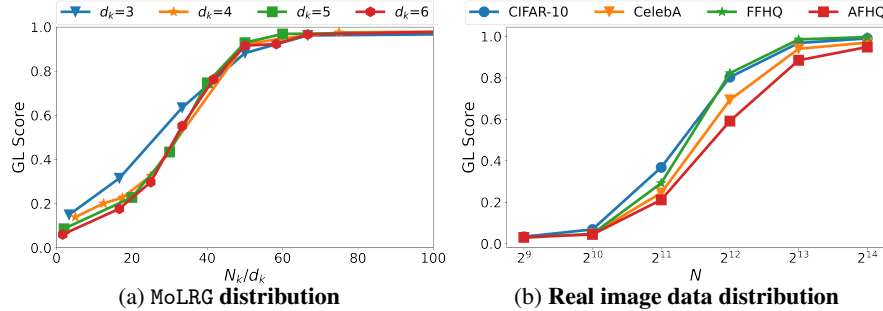


Figure 4: **Phase transition of learning distributions via U-Net.** In (a), the  $x$ -axis is the number of training samples over the intrinsic dimension, while in (b), it is the total number of training samples. The  $y$ -axis is the GL score. We train diffusion models with the U-Net architecture on (a) the data samples generated by the MoLRG distribution with  $K = 2$ ,  $n = 48$  and  $d_k$  varying from 3 to 6 and (b) real image datasets CIFAR-10, CelebA, FFHQ and AFHQ. The GL score is low when U-Net memorizes the training data and high when it learns the underlying distribution.

293 10. Both AFHQ and CelebA align well with our theoretical analysis, which indicates that more  
 294 samples are required for the model to generalize as the intrinsic dimension increases.

## 295 4.2 Semantic Meanings of Low-Dimensional Subspaces

296 In this subsection, we conduct experiments to verify the correspondence between the low-  
 297 dimensional subspaces of the data distribution and the semantics of images on real datasets. We  
 298 denote the Jacobian of the DAE  $\mathbf{x}_\theta(\mathbf{x}_t, t)$  by  $\mathbf{J}_t := \nabla_{\mathbf{x}_t} \mathbf{x}_\theta(\mathbf{x}_t, t) \in \mathbb{R}^{n \times n}$  and let  $\mathbf{J}_t = \mathbf{U}\mathbf{\Sigma}\mathbf{V}^T$   
 299 be an singular value decomposition (SVD) of  $\mathbf{J}_t$ , where  $r = \text{rank}(\mathbf{J}_t)$ ,  $\mathbf{U} = [\mathbf{u}_1, \dots, \mathbf{u}_r] \in \mathcal{O}^{n \times r}$ ,  
 300  $\mathbf{V} = [\mathbf{v}_1, \dots, \mathbf{v}_r] \in \mathcal{O}^{n \times r}$ , and  $\mathbf{\Sigma} = \text{diag}(\sigma_1, \dots, \sigma_r)$  with  $\sigma_1 \geq \dots \geq \sigma_r$  being the singular  
 301 values. To validate the semantic meaning of the basis vectors  $\mathbf{v}_i$ , we vary the value of  $\alpha$  from neg-  
 302 ative to positive and visualize the resulting changes in the generated images. In the experiments,  
 303 we use a pre-trained diffusion denoising probabilistic model (DDPM) [2] on the MetFaces dataset  
 304 [50]. We randomly select an image  $\mathbf{x}_0$  from this dataset and use the reverse process of the diffusion  
 305 denoising implicit model (DDIM) [51] to generate  $\mathbf{x}_t$  at  $t = 0.7T$ , where  $T$  denote the total num-  
 306 ber of time steps. We respectively choose the changed direction as the leading right singular vectors  
 307  $\mathbf{v}_1, \mathbf{v}_3, \mathbf{v}_4, \mathbf{v}_5, \mathbf{v}_6$  and use  $\tilde{\mathbf{x}}_t = \mathbf{x}_t + \alpha \mathbf{v}_i$  to generate new images with  $\alpha \in [-4, 4]$  shown in Figure 8.  
 308 It is observed that these singular vectors enable different semantic edits in terms of gender, hairstyle,  
 309 and color of the image. For comparison, we generate a random unit vector  $\mathbf{s}$  and move  $\mathbf{x}_t$  along  
 310 the direction of  $\mathbf{s}$ , where the editing strength  $\alpha$  is the same as the semantic edits column-wise. The  
 311 results are shown in the last column of Figure 5. Moving along random directions provides minimal  
 312 semantic changes in the generated images, indicating that the low-dimensional subspace spanned  
 313 by  $\mathbf{V}$  is non-trivial and corresponds to semantic meaningful image attributes. More experimental  
 314 results can be found in Figure 8, Figure 9 in Appendix D.3.

## 315 5 Related Works

316 **Learning a mixture of Gaussians via diffusion models.** Recent works have extensively stud-  
 317 ied distribution learning and generalizability of diffusion models for learning a mixture of full-  
 318 rank Gaussian (MoG) model [46, 52, 47, 48, 53]. Specifically, they assumed that there exist centers  
 319  $\boldsymbol{\mu}_1, \dots, \boldsymbol{\mu}_K \in \mathbb{R}^n$  such that image data approximately follows from the following distribution:

$$\mathbf{x} \sim \sum_{k=1}^K \pi_k \mathcal{N}(\boldsymbol{\mu}_k, \mathbf{I}_n), \quad (20)$$

320 where  $\pi_k \geq 0$  is the mixing proportion of the  $k$ -th mixture component satisfying  $\sum_{k=1}^K \pi_k = 1$ .  
 321 Notably, the MoLRG model is distinct from the above MoG model that is widely studied in the litera-  
 322 ture. Specifically, the MoG model consists of multiple Gaussians with varying means and covariance  
 323 spanning the full-dimensional space (see Eq. (20)), while a MoLRG comprises multiple Gaussians  
 324 with zero mean and low-rank covariance (see Eq. (6)), lying in a union of low-dimensional sub-  
 325 spaces. As such, the MoLRG model, inspired by the inherent low-dimensionality of image datasets

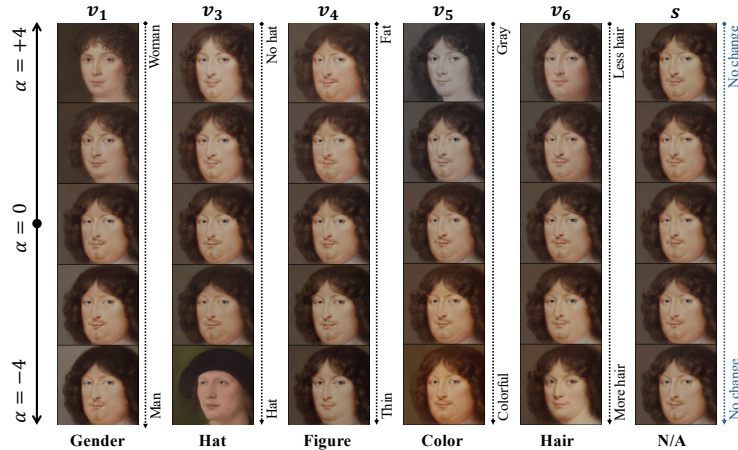


Figure 5: **Correspondence between the singular vectors of the Jacobian of the DAE and semantic image attributes.** We use a pre-trained DDPM with U-Net on the MetFaces dataset [50]. We edit the original image  $x_0$  by changing  $x_t$  into  $x_t + \alpha v_i$ , where  $v_i$  is a singular vector of the Jacobian of the DAE  $x_\theta(x_t, t)$ . In the last column, the editing direction  $s$  is random.

326 [30, 31, 32], offers a deeper insight into how diffusion models can learn underlying distributions in  
 327 practice without suffering from the curse of dimensionality.

328 **Memorization and generalization in diffusion models.** Recently, extensive studies [25, 26, 27]  
 329 empirically revealed that diffusion models learn the score function across two distinct regimes —  
 330 memorization (i.e., learning the empirical distribution) and generalization (i.e., learning the underlying  
 331 distribution) — depending on the training dataset size vs. the model capacity. For a model with  
 332 a fixed number of parameters, there is a phase transition from memorization to generalization as the  
 333 number of training samples increases [25, 27]. Notably, most existing studies on the memorization and  
 334 generalization of diffusion models are empirical. In contrast, our work provides rigorous theoretical  
 335 explanations for these intriguing experimental observations based on the MoLRG model. We  
 336 demonstrate that diffusion models learn the underlying data distribution with the number of training  
 337 samples scaling linearly with the intrinsic dimension.

## 338 6 Conclusion & Discussion

339 In this work, we studied the training loss of diffusion models to investigate when and why diffusion  
 340 models can learn the underlying distribution without suffering from the curse of dimensionality.  
 341 Motivated by extensive empirical observations, we assumed that the underlying data distribution is a  
 342 mixture of low-rank Gaussians. Specifically, we showed that minimizing the training loss is equiv-  
 343 alent to solving the subspace clustering problem under proper network parameterization. Based on  
 344 this equivalence, we further showed that the optimal solutions to the training loss can recover the  
 345 underlying subspaces when the number of samples scales linearly with the intrinsic dimensionality  
 346 of the data distribution. Moreover, we established the correspondence between the subspaces and se-  
 347 mantic representations of image data. Since our studied network parameterization is not sufficiently  
 348 over-parameterized, a future direction is to extend our analysis to an over-parameterized case to fully  
 349 explain the transition from memorization to generalization.

## References

- 350
- 351 [1] Ismail Alkhouri, Shijun Liang, Rongrong Wang, Qing Qu, and Saiprasad Ravishankar.  
352 Diffusion-based adversarial purification for robust deep mri reconstruction. In *ICASSP 2024-  
353 2024 IEEE International Conference on Acoustics, Speech and Signal Processing (ICASSP)*,  
354 pages 12841–12845. IEEE, 2024.
- 355 [2] Jonathan Ho, Ajay Jain, and Pieter Abbeel. Denoising diffusion probabilistic models. *Ad-  
356 vances in Neural Information Processing Systems*, 33:6840–6851, 2020.
- 357 [3] Robin Rombach, Andreas Blattmann, Dominik Lorenz, Patrick Esser, and Björn Ommer.  
358 High-resolution image synthesis with latent diffusion models. In *Proceedings of the IEEE/CVF  
359 Conference on Computer Vision and Pattern Recognition*, pages 10684–10695, 2022.
- 360 [4] Omer Bar-Tal, Hila Chefer, Omer Tov, Charles Herrmann, Roni Paiss, Shiran Zada, Ariel  
361 Ephrat, Junhwa Hur, Yuanzhen Li, Tomer Michaeli, et al. Lumiere: A space-time diffusion  
362 model for video generation. *arXiv preprint arXiv:2401.12945*, 2024.
- 363 [5] Jonathan Ho, William Chan, Chitwan Saharia, Jay Whang, Ruiqi Gao, Alexey Gritsenko,  
364 Diederik P Kingma, Ben Poole, Mohammad Norouzi, David J Fleet, et al. Imagen video:  
365 High definition video generation with diffusion models. *arXiv preprint arXiv:2210.02303*,  
366 2022.
- 367 [6] Jungil Kong, Jaehyeon Kim, and Jaekyoung Bae. HiFi-GAN: Generative adversarial networks  
368 for efficient and high fidelity speech synthesis. *Advances in Neural Information Processing  
369 Systems*, 33:17022–17033, 2020.
- 370 [7] Zhifeng Kong, Wei Ping, Jiaji Huang, Kexin Zhao, and Bryan Catanzaro. DIFFWAVE: A  
371 versatile diffusion model for audio synthesis. In *International Conference on Learning Repre-  
372 sentations*, 2021.
- 373 [8] Hyungjin Chung, Byeongsu Sim, Dohoon Ryu, and Jong Chul Ye. Improving diffusion models  
374 for inverse problems using manifold constraints. *Advances in Neural Information Processing  
375 Systems*, 35:25683–25696, 2022.
- 376 [9] Bowen Song, Soo Min Kwon, Zecheng Zhang, Xinyu Hu, Qing Qu, and Liyue Shen. Solv-  
377 ing inverse problems with latent diffusion models via hard data consistency. In *The Twelfth  
378 International Conference on Learning Representations*, 2024.
- 379 [10] Jascha Sohl-Dickstein, Eric Weiss, Niru Maheswaranathan, and Surya Ganguli. Deep un-  
380 supervised learning using nonequilibrium thermodynamics. In *International Conference on  
381 Machine Learning*, pages 2256–2265. PMLR, 2015.
- 382 [11] Yang Song, Jascha Sohl-Dickstein, Diederik P Kingma, Abhishek Kumar, Stefano Ermon,  
383 and Ben Poole. Score-based generative modeling through stochastic differential equations.  
384 *International Conference on Learning Representations*, 2021.
- 385 [12] Aapo Hyvärinen and Peter Dayan. Estimation of non-normalized statistical models by score  
386 matching. *Journal of Machine Learning Research*, 6(4), 2005.
- 387 [13] Minshuo Chen, Song Mei, Jianqing Fan, and Mengdi Wang. An overview of diffusion  
388 models: Applications, guided generation, statistical rates and optimization. *arXiv preprint  
389 arXiv:2404.07771*, 2024.
- 390 [14] Florinel-Alin Croitoru, Vlad Hondru, Radu Tudor Ionescu, and Mubarak Shah. Diffusion  
391 models in vision: A survey. *IEEE Transactions on Pattern Analysis and Machine Intelligence*,  
392 45(9):10850–10869, 2023.
- 393 [15] Ling Yang, Zhilong Zhang, Yang Song, Shenda Hong, Runsheng Xu, Yue Zhao, Wentao  
394 Zhang, Bin Cui, and Ming-Hsuan Yang. Diffusion models: A comprehensive survey of meth-  
395 ods and applications. *ACM Computing Surveys*, 56(4):1–39, 2023.
- 396 [16] Sitan Chen, Sinho Chewi, Jerry Li, Yuanzhi Li, Adil Salim, and Anru R Zhang. Sampling is  
397 as easy as learning the score: theory for diffusion models with minimal data assumptions. In  
398 *International Conference on Learning Representations*, 2023.

- 399 [17] Holden Lee, Jianfeng Lu, and Yixin Tan. Convergence for score-based generative modeling  
400 with polynomial complexity. *Advances in Neural Information Processing Systems*, 35:22870–  
401 22882, 2022.
- 402 [18] Gen Li, Yuting Wei, Yuxin Chen, and Yuejie Chi. Towards faster non-asymptotic convergence  
403 for diffusion-based generative models. *arXiv preprint arXiv:2306.09251*, 2023.
- 404 [19] Minshuo Chen, Kaixuan Huang, Tuo Zhao, and Mengdi Wang. Score approximation, estima-  
405 tion and distribution recovery of diffusion models on low-dimensional data. In *International  
406 Conference on Machine Learning*, pages 4672–4712. PMLR, 2023.
- 407 [20] Kazusato Oko, Shunta Akiyama, and Taiji Suzuki. Diffusion models are minimax optimal dis-  
408 tribution estimators. In *International Conference on Machine Learning*, pages 26517–26582.  
409 PMLR, 2023.
- 410 [21] Xiangming Gu, Chao Du, Tianyu Pang, Chongxuan Li, Min Lin, and Ye Wang. On memoriza-  
411 tion in diffusion models. *arXiv preprint arXiv:2310.02664*, 2023.
- 412 [22] Gowthami Somepalli, Vasu Singla, Micah Goldblum, Jonas Geiping, and Tom Goldstein. Dif-  
413 fusion art or digital forgery? investigating data replication in diffusion models. In *Proceedings  
414 of the IEEE/CVF Conference on Computer Vision and Pattern Recognition*, pages 6048–6058,  
415 2023.
- 416 [23] Yuxin Wen, Yuchen Liu, Chen Chen, and Lingjuan Lyu. Detecting, explaining, and mitigat-  
417 ing memorization in diffusion models. In *The Twelfth International Conference on Learning  
418 Representations*, 2023.
- 419 [24] Benjamin J Zhang, Siting Liu, Wuchen Li, Markos A Katsoulakis, and Stanley J Osher.  
420 Wasserstein proximal operators describe score-based generative models and resolve memo-  
421 rization. *arXiv preprint arXiv:2402.06162*, 2024.
- 422 [25] Zahra Kadhodaie, Florentin Guth, Eero P Simoncelli, and Stéphane Mallat. Generalization  
423 in diffusion models arises from geometry-adaptive harmonic representations. In *The Twelfth  
424 International Conference on Learning Representations*, 2023.
- 425 [26] TaeHo Yoon, Joo Young Choi, Sehyun Kwon, and Ernest K Ryu. Diffusion probabilistic mod-  
426 els generalize when they fail to memorize. In *ICML 2023 Workshop on Structured Probabilistic  
427 Inference & Generative Modeling*, 2023.
- 428 [27] Huijie Zhang, Jinfan Zhou, Yifu Lu, Minzhe Guo, Peng Wang, Liyue Shen, and Qing Qu. The  
429 emergence of reproducibility and consistency in diffusion models. In *Forty-first International  
430 Conference on Machine Learning*, 2023.
- 431 [28] Sixu Li, Shi Chen, and Qin Li. A good score does not lead to a good generative model. *arXiv  
432 preprint arXiv:2401.04856*, 2024.
- 433 [29] Andre Wibisono, Yihong Wu, and Kaylee Yingxi Yang. Optimal score estimation via empirical  
434 bayes smoothing. *arXiv preprint arXiv:2402.07747*, 2024.
- 435 [30] Sixue Gong, Vishnu Naresh Boddeti, and Anil K Jain. On the intrinsic dimensionality of image  
436 representations. In *Proceedings of the IEEE/CVF Conference on Computer Vision and Pattern  
437 Recognition*, pages 3987–3996, 2019.
- 438 [31] Phil Pope, Chen Zhu, Ahmed Abdelkader, Micah Goldblum, and Tom Goldstein. The intrinsic  
439 dimension of images and its impact on learning. In *International Conference on Learning  
440 Representations*, 2020.
- 441 [32] Jan Pawel Stanczuk, Georgios Batzolis, Teo Deveney, and Carola-Bibiane Schönlieb. Dif-  
442 fusion models encode the intrinsic dimension of data manifolds. In *Forty-first International  
443 Conference on Machine Learning*, 2024.
- 444 [33] Bradley CA Brown, Anthony L Caterini, Brendan Leigh Ross, Jesse C Cresswell, and Gabriel  
445 Loaiza-Ganem. Verifying the union of manifolds hypothesis for image data. In *The Eleventh  
446 International Conference on Learning Representations*, 2023.

- 447 [34] Hamidreza Kamkari, Brendan Leigh Ross, Rasa Hosseinzadeh, Jesse C Cresswell, and Gabriel  
448 Loaiza-Ganem. A geometric view of data complexity: Efficient local intrinsic dimension esti-  
449 mation with diffusion models. *arXiv preprint arXiv:2406.03537*, 2024.
- 450 [35] Gabriel Loaiza-Ganem, Brendan Leigh Ross, Rasa Hosseinzadeh, Anthony L. Caterini, and  
451 Jesse C. Cresswell. Deep generative models through the lens of the manifold hypothesis: A  
452 survey and new connections. *Transactions on Machine Learning Research*, 2024. Survey  
453 Certification, Expert Certification.
- 454 [36] Arnu Pretorius, Steve Kroon, and Herman Kamper. Learning dynamics of linear denoising  
455 autoencoders. In *International Conference on Machine Learning*, pages 4141–4150. PMLR,  
456 2018.
- 457 [37] Pascal Vincent. A connection between score matching and denoising autoencoders. *Neural  
458 computation*, 23(7):1661–1674, 2011.
- 459 [38] Pankaj K Agarwal and Nabil H Mustafa. K-means projective clustering. In *Proceedings of the  
460 23rd ACM SIGMOD-SIGACT-SIGART Symposium on Principles of Database Systems*, pages  
461 155–165, 2004.
- 462 [39] René Vidal. Subspace clustering. *IEEE Signal Processing Magazine*, 28(2):52–68, 2011.
- 463 [40] Peng Wang, Huikang Liu, Anthony Man-Cho So, and Laura Balzano. Convergence and recov-  
464 ery guarantees of the k-subspaces method for subspace clustering. In *International Conference  
465 on Machine Learning*, pages 22884–22918. PMLR, 2022.
- 466 [41] Tero Karras, Miika Aittala, Timo Aila, and Samuli Laine. Elucidating the design space  
467 of diffusion-based generative models. *Advances in Neural Information Processing Systems*,  
468 35:26565–26577, 2022.
- 469 [42] Brian DO Anderson. Reverse-time diffusion equation models. *Stochastic Processes and their  
470 Applications*, 12(3):313–326, 1982.
- 471 [43] Xinlei Chen, Zhuang Liu, Saining Xie, and Kaiming He. Deconstructing denoising diffusion  
472 models for self-supervised learning. *arXiv preprint arXiv:2401.14404*, 2024.
- 473 [44] Weilai Xiang, Hongyu Yang, Di Huang, and Yunhong Wang. Denoising diffusion autoencoders  
474 are unified self-supervised learners. In *Proceedings of the IEEE/CVF International Conference  
475 on Computer Vision*, pages 15802–15812, 2023.
- 476 [45] Olga Russakovsky, Jia Deng, Hao Su, Jonathan Krause, Sanjeev Satheesh, Sean Ma, Zhiheng  
477 Huang, Andrej Karpathy, Aditya Khosla, Michael Bernstein, et al. Imagenet large scale visual  
478 recognition challenge. *International journal of computer vision*, 115:211–252, 2015.
- 479 [46] Sitan Chen, Vasilis Kontonis, and Kulin Shah. Learning general gaussian mixtures with effi-  
480 cient score matching. *arXiv preprint arXiv:2404.18893*, 2024.
- 481 [47] Khashayar Gatmiry, Jonathan Kelner, and Holden Lee. Learning mixtures of gaussians using  
482 diffusion models. *arXiv preprint arXiv:2404.18869*, 2024.
- 483 [48] Kulin Shah, Sitan Chen, and Adam Klivans. Learning mixtures of gaussians using the DDPM  
484 objective. *Advances in Neural Information Processing Systems*, 36:19636–19649, 2023.
- 485 [49] Olaf Ronneberger, Philipp Fischer, and Thomas Brox. U-net: Convolutional networks  
486 for biomedical image segmentation. In *Medical image computing and computer-assisted  
487 intervention–MICCAI 2015: 18th international conference, Munich, Germany, October 5-9,  
488 2015, proceedings, part III 18*, pages 234–241. Springer, 2015.
- 489 [50] Tero Karras, Miika Aittala, Janne Hellsten, Samuli Laine, Jaakko Lehtinen, and Timo Aila.  
490 Training generative adversarial networks with limited data. In *Proceedings of the 34th Inter-  
491 national Conference on Neural Information Processing Systems, NIPS ’20*, Red Hook, NY,  
492 USA, 2020. Curran Associates Inc.
- 493 [51] Jiaming Song, Chenlin Meng, and Stefano Ermon. Denoising diffusion implicit models. In  
494 *International Conference on Learning Representations*, 2020.

- 495 [52] Frank Cole and Yulong Lu. Score-based generative models break the curse of dimensionality  
496 in learning a family of sub-gaussian distributions. In *The Twelfth International Conference on*  
497 *Learning Representations*, 2024.
- 498 [53] Yuchen Wu, Minshuo Chen, Zihao Li, Mengdi Wang, and Yuting Wei. Theoretical insights  
499 for diffusion guidance: A case study for gaussian mixture models. In *Forty-first International*  
500 *Conference on Machine Learning*, 2024.
- 501 [54] Per-Åke Wedin. Perturbation bounds in connection with singular value decomposition. *BIT*  
502 *Numerical Mathematics*, 12:99–111, 1972.
- 503 [55] Calvin Luo. Understanding diffusion models: A unified perspective. *arXiv preprint*  
504 *arXiv:2208.11970*, 2022.
- 505 [56] Alex Krizhevsky, Geoffrey Hinton, et al. Learning multiple layers of features from tiny images.  
506 2009.
- 507 [57] Ziwei Liu, Ping Luo, Xiaogang Wang, and Xiaoou Tang. Deep learning face attributes in the  
508 wild. In *Proceedings of the IEEE international conference on computer vision*, pages 3730–  
509 3738, 2015.
- 510 [58] Vahid Kazemi and Josephine Sullivan. One millisecond face alignment with an ensemble  
511 of regression trees. In *Proceedings of the IEEE conference on computer vision and pattern*  
512 *recognition*, pages 1867–1874, 2014.
- 513 [59] Yunjey Choi, Youngjung Uh, Jaejun Yoo, and Jung-Woo Ha. Stargan v2: Diverse image  
514 synthesis for multiple domains. In *Proceedings of the IEEE/CVF conference on computer*  
515 *vision and pattern recognition*, pages 8188–8197, 2020.
- 516 [60] Ed Pizzi, Sreya Dutta Roy, Sugosh Nagavara Ravindra, Priya Goyal, and Matthijs Douze. A  
517 self-supervised descriptor for image copy detection. In *Proceedings of the IEEE/CVF Confer-*  
518 *ence on Computer Vision and Pattern Recognition*, pages 14532–14542, 2022.
- 519 [61] Diederik P Kingma and Jimmy Ba. Adam: A method for stochastic optimization. *arXiv*  
520 *preprint arXiv:1412.6980*, 2014.
- 521 [62] Mark Rudelson and Roman Vershynin. Smallest singular value of a random rectangular matrix.  
522 *Communications on Pure and Applied Mathematics: A Journal Issued by the Courant Institute*  
523 *of Mathematical Sciences*, 62(12):1707–1739, 2009.
- 524 [63] Roman Vershynin. *High-dimensional probability: An introduction with applications in data*  
525 *science*, volume 47. Cambridge university press, 2018.

## Supplementary Material

526  
527

528 In the appendix, the organization is as follows. We first provide proof details for Section 2 and  
529 Section 3 in Appendix A and Appendix B, respectively. Then, we present our experimental setups  
530 for Figure 2 in Appendix C and for Section 4 in Appendix D. Finally, some auxiliary results for  
531 proving the main theorems are provided in Appendix E.

532 To simplify our development, we introduce some further notation. We denote by  $\mathcal{N}(\boldsymbol{\mu}, \boldsymbol{\Sigma})$  a multi-  
533 variate Gaussian distribution with mean  $\boldsymbol{\mu} \in \mathbb{R}^n$  and covariance  $\boldsymbol{\Sigma} \succeq \mathbf{0}$ . Given a Gaussian random  
534 vector  $\boldsymbol{x} \sim \mathcal{N}(\boldsymbol{\mu}, \boldsymbol{\Sigma})$ , if  $\boldsymbol{\Sigma} \succ \mathbf{0}$ , with abuse of notation, we write its pdf as

$$\mathcal{N}(\boldsymbol{x}; \boldsymbol{\mu}, \boldsymbol{\Sigma}) := \frac{1}{(2\pi)^{n/2} \det^{1/2}(\boldsymbol{\Sigma})} \exp\left(-\frac{1}{2}(\boldsymbol{x} - \boldsymbol{\mu})^T \boldsymbol{\Sigma}^{-1}(\boldsymbol{x} - \boldsymbol{\mu})\right). \quad (21)$$

535 If a random vector  $\boldsymbol{x} \in \mathbb{R}^n$  satisfies  $\boldsymbol{x} \sim \mathcal{N}(\boldsymbol{\mu}, \boldsymbol{U}\boldsymbol{U}^T)$  for some  $\boldsymbol{\mu} \in \mathbb{R}^n$  and  $\boldsymbol{U} \in \mathcal{O}^{n \times d}$ , we have

$$\boldsymbol{x} = \boldsymbol{\mu} + \boldsymbol{U}\boldsymbol{a}, \quad (22)$$

536 where  $\boldsymbol{a} \sim \mathcal{N}(\mathbf{0}, \boldsymbol{I}_d)$ . Therefore, a mixture of low-rank Gaussians in Definition 1 can be expressed  
537 as

$$\mathbb{P}(\boldsymbol{x} = \boldsymbol{U}_k^* \boldsymbol{a}_k) = \pi_k, \text{ where } \boldsymbol{a}_k \sim \mathcal{N}(\mathbf{0}, \boldsymbol{I}_{d_k}), \forall k \in [K]. \quad (23)$$

### 538 A Proofs in Section 2

#### 539 A.1 Relation between Score Matching Loss and Denoiser Autoencoder Loss

540 To estimate  $\nabla \log p_t(\boldsymbol{x})$ , one can train a time-dependent score-based model  $\boldsymbol{s}_\theta(\boldsymbol{x}, t)$  via minimizing  
541 the following objective [11]:

$$\min_{\boldsymbol{\theta}} \int_0^1 \xi_t \mathbb{E}_{\boldsymbol{x}_0 \sim p_{\text{data}}} \mathbb{E}_{\boldsymbol{x}_t | \boldsymbol{x}_0} \left[ \|\boldsymbol{s}_\theta(\boldsymbol{x}_t, t) - \nabla \log p_t(\boldsymbol{x}_t | \boldsymbol{x}_0)\|^2 \right] dt, \quad (24)$$

542 where  $\xi_t : [0, 1] \rightarrow \mathbb{R}^+$  is a positive weighting function. Let  $\boldsymbol{x}_\theta(\cdot, t) : \mathbb{R}^d \times [0, 1] \rightarrow \mathbb{R}^d$  de-  
543 note a neural network parameterized by parameters  $\boldsymbol{\theta}$  to approximate  $\mathbb{E}[\boldsymbol{x}_0 | \boldsymbol{x}_t]$ . According to the  
544 Tweedie's formula (4),  $\boldsymbol{s}_\theta(\boldsymbol{x}_t, t) = (s_t \boldsymbol{x}_\theta(\boldsymbol{x}_t, t) - \boldsymbol{x}_t) / \gamma_t^2$  can be used to estimate score functions.  
545 Substituting this and  $\nabla \log p_t(\boldsymbol{x}_t | \boldsymbol{x}_0) = (s_t \boldsymbol{x}_0 - \boldsymbol{x}_t) / \gamma_t^2$  due to (2) yields

$$\begin{aligned} & \min_{\boldsymbol{\theta}} \int_0^1 \xi_t \mathbb{E}_{\boldsymbol{x}_0 \sim p_{\text{data}}} \mathbb{E}_{\boldsymbol{x}_t | \boldsymbol{x}_0} \left[ \left\| \frac{1}{\gamma_t^2} (s_t \boldsymbol{x}_\theta(\boldsymbol{x}_t, t) - \boldsymbol{x}_t) - \frac{1}{\gamma_t^2} (s_t \boldsymbol{x}_0 - \boldsymbol{x}_t) \right\|^2 \right] dt \\ & = \int_0^1 \frac{\xi_t}{s_t^2 \sigma_t^4} \mathbb{E}_{\boldsymbol{x}_0 \sim p_{\text{data}}} \mathbb{E}_{\boldsymbol{\epsilon} \sim \mathcal{N}(\mathbf{0}, \boldsymbol{I}_n)} \left[ \|\boldsymbol{x}_\theta(s_t \boldsymbol{x}_0 + \gamma_t \boldsymbol{\epsilon}, t) - \boldsymbol{x}_0\|^2 \right] dt, \end{aligned}$$

546 where the equality follows from  $\boldsymbol{x}_t = s_t \boldsymbol{x}_0 + \gamma_t \boldsymbol{\epsilon}$  due to (2). Then, we obtain

$$\min_{\boldsymbol{\theta}} \int_0^1 \lambda_t \mathbb{E}_{\boldsymbol{x}_0 \sim p_{\text{data}}} \mathbb{E}_{\boldsymbol{\epsilon} \sim \mathcal{N}(\mathbf{0}, \boldsymbol{I}_n)} \left[ \|\boldsymbol{x}_\theta(s_t \boldsymbol{x}_0 + \gamma_t \boldsymbol{\epsilon}, t) - \boldsymbol{x}_0\|^2 \right] dt, \quad (25)$$

547 where  $\lambda_t = \xi_t / (s_t^2 \sigma_t^4)$ . However, only data points  $\{\boldsymbol{x}^{(i)}\}_{i=1}^N$  sampled from the underlying data  
548 distribution  $p_{\text{data}}$  are available in practice. Therefore, we study the following empirical counterpart  
549 of Problem (25) over the training samples, i.e., Problem (5). We refer the reader to [25, Section 2.1]  
550 for more discussions on the denoising error of this problem.

#### 551 A.2 Proof of in Lemma 1

552 Assuming that the underlying data distribution follows a mixture of low-rank Gaussians as defined  
553 in Definition 1, we first compute the ground-truth score function as follows.

554 **Proposition 1.** *Suppose that the underlying data distribution  $p_{\text{data}}$  follows a mixture of low-rank*  
555 *Gaussian distributions in Definition 1. In the forward process of diffusion models, the pdf of  $\boldsymbol{x}_t$  for*  
556 *each  $t > 0$  is*

$$p_t(\boldsymbol{x}) = \sum_{k=1}^K \pi_k \mathcal{N}(\boldsymbol{x}; \mathbf{0}, s_t^2 \boldsymbol{U}_k^* \boldsymbol{U}_k^{*T} + \gamma_t^2 \boldsymbol{I}_n), \quad (26)$$

557 where  $\gamma_t = s_t \sigma_t$ . Moreover, the score function of  $p_t(\mathbf{x})$  is

$$\nabla \log p_t(\mathbf{x}) = -\frac{1}{\gamma_t^2} \left( \mathbf{x} - \frac{s_t^2}{s_t^2 + \gamma_t^2} \frac{\sum_{k=1}^K \pi_k \mathcal{N}(\mathbf{x}; \mathbf{0}, s_t^2 \mathbf{U}_k^* \mathbf{U}_k^{*T} + \gamma_t^2 \mathbf{I}_n) \mathbf{U}_k^* \mathbf{U}_k^{*T} \mathbf{x}}{\sum_{k=1}^K \pi_k \mathcal{N}(\mathbf{x}; \mathbf{0}, s_t^2 \mathbf{U}_k^* \mathbf{U}_k^{*T} + \gamma_t^2 \mathbf{I}_n)} \right). \quad (27)$$

558 *Proof.* Let  $Y \in \{1, \dots, K\}$  be a discrete random variable that denotes the value of components of  
 559 the mixture model. Note that  $\gamma_t = s_t \sigma_t$ . It follows from Definition 1 that  $\mathbb{P}(Y = k) = \pi_k$  for each  
 560  $k \in [K]$ . We first compute

$$\begin{aligned} p_t(\mathbf{x}|Y = k) &= \int p_t(\mathbf{x}|Y = k, \mathbf{a}_k) \mathcal{N}(\mathbf{a}_k; \mathbf{0}, \mathbf{I}_{d_k}) d\mathbf{a}_k = \int p_t(\mathbf{x}|\mathbf{x}_0 = \mathbf{U}_k^* \mathbf{a}_k) \mathcal{N}(\mathbf{a}_k; \mathbf{0}, \mathbf{I}_{d_k}) d\mathbf{a}_k \\ &= \int \mathcal{N}(\mathbf{x}; s_t \mathbf{U}_k^* \mathbf{a}_k, \gamma_t^2 \mathbf{I}_n) \mathcal{N}(\mathbf{a}_k; \mathbf{0}, \mathbf{I}_{d_k}) d\mathbf{a}_k \\ &= \frac{1}{(2\pi)^{n/2} (2\pi)^{d_k/2} \gamma_t^{d_k}} \int \exp\left(-\frac{1}{2\gamma_t^2} \|\mathbf{x} - s_t \mathbf{U}_k^* \mathbf{a}_k\|^2\right) \exp\left(-\frac{1}{2} \|\mathbf{a}_k\|^2\right) d\mathbf{a}_k \\ &= \frac{1}{(2\pi)^{n/2} \gamma_t^{d_k}} \left(\frac{s_t^2 + \gamma_t^2}{\gamma_t^2}\right)^{-d_k/2} \exp\left(-\frac{1}{2\gamma_t^2} \mathbf{x}^T \left(\mathbf{I}_n - \frac{s_t^2}{s_t^2 + \gamma_t^2} \mathbf{U}_k^* \mathbf{U}_k^{*T}\right) \mathbf{x}\right) \\ &\quad \int \frac{1}{(2\pi)^{d_k/2}} \left(\frac{\gamma_t^2}{s_t^2 + \gamma_t^2}\right)^{-d_k/2} \exp\left(-\frac{s_t^2 + \gamma_t^2}{2\gamma_t^2} \left\| \mathbf{a}_k - \frac{s_t}{s_t^2 + \gamma_t^2} \mathbf{U}_k^{*T} \mathbf{x} \right\|^2\right) d\mathbf{a}_k \\ &= \frac{1}{(2\pi)^{n/2}} \frac{1}{\left((s_t^2 + \gamma_t^2)^d \gamma_t^{2(n-d)}\right)^{1/2}} \exp\left(-\frac{1}{2\gamma_t^2} \mathbf{x}^T \left(\mathbf{I}_n - \frac{s_t^2}{s_t^2 + \gamma_t^2} \mathbf{U}_k^* \mathbf{U}_k^{*T}\right) \mathbf{x}\right) \\ &= \frac{1}{(2\pi)^{n/2} \det^{1/2}(s_t^2 \mathbf{U}_k^* \mathbf{U}_k^{*T} + \gamma_t^2 \mathbf{I}_n)} \exp\left(-\frac{1}{2} \mathbf{x}^T (s_t^2 \mathbf{U}_k^* \mathbf{U}_k^{*T} + \gamma_t^2 \mathbf{I}_n)^{-1} \mathbf{x}\right) \\ &= \mathcal{N}(\mathbf{x}; \mathbf{0}, s_t^2 \mathbf{U}_k^* \mathbf{U}_k^{*T} + \gamma_t^2 \mathbf{I}_n), \end{aligned}$$

561 where the second equality follows from (2), the third equality uses (21), the fourth equality is due  
 562 to the fact that  $\langle \mathbf{x}, \mathbf{U}_k^* \mathbf{a} \rangle$  is an odd function, and the second to last equality uses  $\det(s_t^2 \mathbf{U}_k^* \mathbf{U}_k^{*T} +$   
 563  $\gamma_t^2 \mathbf{I}_n) = (s_t^2 + \gamma_t^2)^d \gamma_t^{2(n-d)}$  and  $(s_t^2 \mathbf{U}_k^* \mathbf{U}_k^{*T} + \gamma_t^2 \mathbf{I}_n)^{-1} = (\mathbf{I}_n - s_t^2 / (s_t^2 + \gamma_t^2) \mathbf{U}_k^* \mathbf{U}_k^{*T}) / \gamma_t^2$  due  
 564 to the matrix inversion lemma and  $\mathbf{U}_k^{*T} \mathbf{U}_k^* = \mathbf{I}_{d_k}$ . This, together with  $\mathbb{P}(Y = k) = \pi_k$  for each  
 565  $k \in [K]$ , yields

$$p_t(\mathbf{x}) = \sum_{k=1}^K p_t(\mathbf{x}|Y = k) \mathbb{P}(Y = k) = \sum_{k=1}^K \pi_k \mathcal{N}(\mathbf{x}; \mathbf{0}, s_t^2 \mathbf{U}_k^* \mathbf{U}_k^{*T} + \gamma_t^2 \mathbf{I}_n).$$

566 Next, we directly compute

$$\begin{aligned} \nabla \log p_t(\mathbf{x}) &= \frac{\nabla p_t(\mathbf{x})}{p_t(\mathbf{x})} = \frac{\sum_{k=1}^K \pi_k \mathcal{N}(\mathbf{x}; \mathbf{0}, s_t^2 \mathbf{U}_k^* \mathbf{U}_k^{*T} + \gamma_t^2 \mathbf{I}_n) \left(-\frac{1}{\gamma_t^2} \mathbf{x} + \frac{s_t^2}{\gamma_t^2 (s_t^2 + \gamma_t^2)} \mathbf{U}_k^* \mathbf{U}_k^{*T} \mathbf{x}\right)}{\sum_{k=1}^K \pi_k \mathcal{N}(\mathbf{x}; \mathbf{0}, s_t^2 \mathbf{U}_k^* \mathbf{U}_k^{*T} + \gamma_t^2 \mathbf{I}_n)} \\ &= -\frac{1}{\gamma_t^2} \left( \mathbf{x} - \frac{s_t^2}{s_t^2 + \gamma_t^2} \frac{\sum_{k=1}^K \pi_k \mathcal{N}(\mathbf{x}; \mathbf{0}, s_t^2 \mathbf{U}_k^* \mathbf{U}_k^{*T} + \gamma_t^2 \mathbf{I}_n) \mathbf{U}_k^* \mathbf{U}_k^{*T} \mathbf{x}}{\sum_{k=1}^K \pi_k \mathcal{N}(\mathbf{x}; \mathbf{0}, s_t^2 \mathbf{U}_k^* \mathbf{U}_k^{*T} + \gamma_t^2 \mathbf{I}_n)} \right). \end{aligned}$$

567

□

568 *Proof of Lemma 1.* According to (4) and Proposition 1, we compute

$$\begin{aligned}
\mathbb{E}[\mathbf{x}_0|\mathbf{x}_t] &= \frac{\mathbf{x}_t + \gamma_t^2 \nabla \log p_t(\mathbf{x}_t)}{s_t} = \frac{s_t}{s_t^2 + \gamma_t^2} \frac{\sum_{k=1}^K \pi_k \mathcal{N}(\mathbf{x}; \mathbf{0}, s_t^2 \mathbf{U}_k^* \mathbf{U}_k^{*T} + \gamma_t^2 \mathbf{I}_n) \mathbf{U}_k^* \mathbf{U}_k^{*T} \mathbf{x}_t}{\sum_{k=1}^K \pi_k \mathcal{N}(\mathbf{x}_t; \mathbf{0}, s_t^2 \mathbf{U}_k^* \mathbf{U}_k^{*T} + \gamma_t^2 \mathbf{I}_n)} \\
&= \frac{s_t}{s_t^2 + \gamma_t^2} \frac{\sum_{k=1}^K \pi_k \exp\left(-\frac{1}{2\gamma_t^2} \left(\|\mathbf{x}_t\|^2 - \frac{s_t^2}{s_t^2 + \gamma_t^2} \|\mathbf{U}_k^{*T} \mathbf{x}_t\|^2\right)\right) \mathbf{U}_k^* \mathbf{U}_k^{*T} \mathbf{x}_t}{\sum_{k=1}^K \pi_k \exp\left(-\frac{1}{2\gamma_t^2} \left(\|\mathbf{x}_t\|^2 - \frac{s_t^2}{s_t^2 + \gamma_t^2} \|\mathbf{U}_k^{*T} \mathbf{x}_t\|^2\right)\right)} \\
&= \frac{s_t}{s_t^2 + \gamma_t^2} \frac{\sum_{k=1}^K \pi_k \exp\left(\frac{1}{2\gamma_t^2} \frac{s_t^2}{s_t^2 + \gamma_t^2} \|\mathbf{U}_k^{*T} \mathbf{x}_t\|^2\right) \mathbf{U}_k^* \mathbf{U}_k^{*T} \mathbf{x}_t}{\sum_{k=1}^K \pi_k \exp\left(\frac{1}{2\gamma_t^2} \frac{s_t^2}{s_t^2 + \gamma_t^2} \|\mathbf{U}_k^{*T} \mathbf{x}_t\|^2\right)},
\end{aligned}$$

569 where the third equality uses (21) and  $(s_t^2 \mathbf{U}_k^* \mathbf{U}_k^{*T} + \gamma_t^2 \mathbf{I}_n)^{-1} = (\mathbf{I}_n - s_t^2 / (s_t^2 + \gamma_t^2) \mathbf{U}_k^* \mathbf{U}_k^{*T}) / \gamma_t^2$   
570 due to the matrix inversion lemma.  $\square$

### 571 A.3 Proof of Theorem 1

572 *Proof of Theorem 1.* Plugging (10) into the integrand of (5) yields

$$\begin{aligned}
&\mathbb{E}_\epsilon \left[ \left\| \frac{s_t}{s_t^2 + \gamma_t^2} \mathbf{U} \mathbf{U}^T (s_t \mathbf{x}^{(i)} + \gamma_t \boldsymbol{\epsilon}) - \mathbf{x}^{(i)} \right\|^2 \right] \\
&= \left\| \frac{s_t^2}{s_t^2 + \gamma_t^2} \mathbf{U} \mathbf{U}^T \mathbf{x}^{(i)} - \mathbf{x}^{(i)} \right\|^2 + \frac{(s_t \gamma_t)^2}{(s_t^2 + \gamma_t^2)^2} \mathbb{E}_\epsilon [\|\mathbf{U} \mathbf{U}^T \boldsymbol{\epsilon}\|^2] \\
&= \left\| \frac{s_t^2}{s_t^2 + \gamma_t^2} \mathbf{U} \mathbf{U}^T \mathbf{x}^{(i)} - \mathbf{x}^{(i)} \right\|^2 + \frac{(s_t \gamma_t)^2 d}{(s_t^2 + \gamma_t^2)^2},
\end{aligned}$$

573 where the first equality follows from  $\mathbb{E}_\epsilon[\langle \mathbf{x}, \boldsymbol{\epsilon} \rangle] = 0$  for any given  $\mathbf{x} \in \mathbb{R}^n$  due to  $\boldsymbol{\epsilon} \sim \mathcal{N}(\mathbf{0}, \mathbf{I}_n)$ ,  
574 and the second equality uses  $\mathbb{E}_\epsilon [\|\mathbf{U} \mathbf{U}^T \boldsymbol{\epsilon}\|^2] = \mathbb{E}_\epsilon [\|\mathbf{U}^T \boldsymbol{\epsilon}\|^2] = \sum_{i=1}^d \mathbb{E}_\epsilon [\|\mathbf{u}_i^T \boldsymbol{\epsilon}\|^2] = d$  due to  
575  $\mathbf{U} \in \mathcal{O}^{n \times d}$  and  $\boldsymbol{\epsilon} \sim \mathcal{N}(\mathbf{0}, \mathbf{I}_n)$ . This, together with  $\gamma_t = s_t \sigma_t$  and (5), yields

$$\ell(\mathbf{U}) = \frac{1}{N} \sum_{i=1}^N \int_0^1 \lambda_t \left( \|\mathbf{x}^{(i)}\|^2 - \frac{1 + 2\sigma_t^2}{(1 + \sigma_t^2)^2} \|\mathbf{U}^T \mathbf{x}^{(i)}\|^2 + \frac{\sigma_t^2 d}{(1 + \sigma_t^2)^2} \right) dt,$$

576 Obviously, minimizing the above function in terms of  $\mathbf{U}$  amounts to

$$\min_{\mathbf{U}^T \mathbf{U} = \mathbf{I}_d} - \int_0^1 \frac{(1 + 2\sigma_t^2) \lambda_t}{(1 + \sigma_t^2)^2} dt \frac{1}{N} \sum_{i=1}^N \|\mathbf{U}^T \mathbf{x}^{(i)}\|^2,$$

577 which is equivalent to Problem (11).  $\square$

### 578 A.4 Proof of Theorem 2

579 *Proof of Theorem 2.* For ease of exposition, let

$$\mathbf{X} = [\mathbf{x}^{(1)} \quad \dots \quad \mathbf{x}^{(N)}] \in \mathbb{R}^{n \times N}, \quad \mathbf{A} = [\mathbf{a}_1 \quad \dots \quad \mathbf{a}_N] \in \mathbb{R}^{d \times N}, \quad \mathbf{E} = [\mathbf{e}_1 \quad \dots \quad \mathbf{e}_N] \in \mathbb{R}^{n \times N}.$$

580 Using this and (9), we obtain

$$\mathbf{X} = \mathbf{U}^* \mathbf{A} + \mathbf{E}. \tag{28}$$

581 Let  $r_A := \text{rank}(\mathbf{A}) \leq \min\{d, N\}$  and  $\mathbf{A} = \mathbf{U}_A \boldsymbol{\Sigma}_A \mathbf{V}_A^T$  be an singular value decomposition (SVD)  
582 of  $\mathbf{A}$ , where  $\mathbf{U}_A \in \mathcal{O}^{d \times r_A}$ ,  $\mathbf{V}_A \in \mathcal{O}^{N \times r_A}$ , and  $\boldsymbol{\Sigma}_A \in \mathbb{R}^{r_A \times r_A}$ . It follows from Theorem 1 that  
583 Problem (5) with the parameterization (10) is equivalent to Problem (11).

584 (i) Suppose that  $N \geq d$ . Applying Lemma 3 with  $\varepsilon = 1/(2c_1)$  to  $\mathbf{A} \in \mathbb{R}^{d \times N}$ , it holds with  
 585 probability at least  $1 - 1/2^{N-d+1} - \exp(-c_2N)$  that

$$\sigma_{\min}(\mathbf{A}) = \sigma_d(\mathbf{A}) \geq \frac{\sqrt{N} - \sqrt{d-1}}{2c_1}, \quad (29)$$

586 where  $c_1, c_2 > 0$  are constants depending polynomially only on the Gaussian moment. This implies  
 587  $r_A = d$  and  $\mathbf{U}_A \in \mathcal{O}^d$ . Since Problem (11) is a PCA problem, the columns of any optimal solution  
 588  $\hat{\mathbf{U}} \in \mathcal{O}^{n \times d}$  consist of left singular vectors associated with the top  $d$  singular values of  $\mathbf{X}$ . This,  
 589 together with Wedin's Theorem [54] and (28), yields

$$\left\| \hat{\mathbf{U}}\hat{\mathbf{U}}^T - \mathbf{U}^*\mathbf{U}^{*T} \right\|_F = \left\| \hat{\mathbf{U}}\hat{\mathbf{U}}^T - (\mathbf{U}^*\mathbf{U}_A)(\mathbf{U}^*\mathbf{U}_A)^T \right\|_F \leq \frac{2\|\mathbf{E}\|_F}{\sigma_{\min}(\mathbf{A})} = \frac{4c_1\|\mathbf{E}\|_F}{\sqrt{N} - \sqrt{d-1}}.$$

590 This, together with absorbing 4 into  $c_1$ , yields (12).

591 (ii) Suppose that  $N < d$ . According to Lemma 3 with  $\varepsilon = 1/(2c_1)$ , it holds with probability at least  
 592  $1 - 1/2^{d-N+1} - \exp(-c_2d)$  that

$$\sigma_{\min}(\mathbf{A}) = \sigma_N(\mathbf{A}) \geq \frac{\sqrt{d} - \sqrt{N-1}}{2c_1}, \quad (30)$$

593 where  $c_1, c_2 > 0$  are constants depending polynomially only on the Gaussian moment. This implies  
 594  $r_A = N$  and  $\mathbf{U}_A \in \mathcal{O}^{d \times N}$ . This, together with the fact that  $\mathbf{A} = \mathbf{U}_A \boldsymbol{\Sigma}_A \mathbf{V}_A^T$  is an SVD of  $\mathbf{A}$ , yields  
 595 that  $\mathbf{U}^* \mathbf{A} = (\mathbf{U}^* \mathbf{U}_A) \boldsymbol{\Sigma}_A \mathbf{V}_A^T$  is an SVD of  $\mathbf{U}^* \mathbf{A}$  with  $\mathbf{U}^* \mathbf{U}_A \in \mathcal{O}^{n \times N}$ . Note that  $\text{rank}(\mathbf{X}) \leq N$ .  
 596 Let  $\mathbf{X} = \mathbf{U}_X \boldsymbol{\Sigma}_X \mathbf{V}_X^T$  be an SVD of  $\mathbf{X}$ , where  $\mathbf{U}_X \in \mathcal{O}^{n \times N}$ ,  $\mathbf{V}_X \in \mathcal{O}^N$ , and  $\boldsymbol{\Sigma}_X \in \mathbb{R}^{N \times N}$ . This,  
 597 together with Wedin's Theorem [54] and (30), yields

$$\left\| \mathbf{U}_X \mathbf{U}_X^T - \mathbf{U}^* \mathbf{U}_A \mathbf{U}_A^T \mathbf{U}^{*T} \right\|_F \leq \frac{2\|\mathbf{E}\|_F}{\sigma_{\min}(\mathbf{A})} = \frac{4c_1\|\mathbf{E}\|_F}{\sqrt{d} - \sqrt{N-1}}. \quad (31)$$

598 Note that Problem (11) has infinite optimal solutions when  $N < d$ , which take the form of

$$\hat{\mathbf{U}} = [\mathbf{U}_X \quad \bar{\mathbf{U}}_X] \in \mathcal{O}^{n \times d}.$$

599 Now, we consider that  $\bar{\mathbf{U}}_X \in \mathcal{O}^{n \times (d-N)}$  is an optimal solution of the following problem:

$$\min_{\mathbf{V} \in \mathcal{O}^{n \times (d-N)}, \mathbf{U}_X^T \mathbf{V} = \mathbf{0}} \left\| \mathbf{V}^T \mathbf{U}^* (\mathbf{I} - \mathbf{U}_A \mathbf{U}_A^T) \right\|_F^2. \quad (32)$$

600 Then, one can verify that the rank of the following matrix is at most  $d$ :

$$\mathbf{B} := [\mathbf{U}_X \quad \mathbf{U}^* (\mathbf{I} - \mathbf{U}_A \mathbf{U}_A^T)]$$

601 Then, if  $n \geq 2d - N$ , it is easy to see that the optimal value of Problem (32) is 0. If  $n < 2d - N$ ,  
 602 the optima value is achieved at  $\mathbf{V}^* = [\mathbf{V}_1^* \quad \mathbf{V}_2^*]$  with  $\mathbf{V}_1^* \in \mathbb{R}^{n \times (n-d)}$  and  $\mathbf{V}_2^* \in \mathbb{R}^{n \times (2d-N-n)}$   
 603 satisfying  $\mathbf{V}_1^{*T} \mathbf{B} = \mathbf{0}$ , which implies

$$\left\| \mathbf{V}^{*T} \mathbf{U}^* (\mathbf{I} - \mathbf{U}_A \mathbf{U}_A^T) \right\|_F^2 = \left\| \mathbf{V}_2^{*T} \mathbf{U}^* (\mathbf{I} - \mathbf{U}_A \mathbf{U}_A^T) \right\|_F^2 \leq 2d - N - n.$$

604 Consequently, the optimal value of Problem (32) is less than

$$\max \{0, 2d - (n + N)\} \quad (33)$$

605 Then, we obtain that

$$\begin{aligned} \left\| \hat{\mathbf{U}}\hat{\mathbf{U}}^T - \mathbf{U}^*\mathbf{U}^{*T} \right\|_F &= \left\| \mathbf{U}_X \mathbf{U}_X^T + \bar{\mathbf{U}}_X \bar{\mathbf{U}}_X^T - \mathbf{U}^* \mathbf{U}_A \mathbf{U}_A^T \mathbf{U}^{*T} - \mathbf{U}^* (\mathbf{I} - \mathbf{U}_A \mathbf{U}_A^T) \mathbf{U}^{*T} \right\|_F \\ &\geq \left\| \bar{\mathbf{U}}_X \bar{\mathbf{U}}_X^T - \mathbf{U}^* (\mathbf{I} - \mathbf{U}_A \mathbf{U}_A^T) \mathbf{U}^{*T} \right\|_F - \left\| \mathbf{U}_X \mathbf{U}_X^T - \mathbf{U}^* \mathbf{U}_A \mathbf{U}_A^T \mathbf{U}^{*T} \right\|_F \\ &\geq \sqrt{2(d-N) - 2 \max \{0, 2d - (n + N)\}} - \frac{4c_1\|\mathbf{E}\|_F}{\sqrt{d} - \sqrt{N-1}} \\ &\geq \sqrt{2 \min \{d - N, n - d\}} - \frac{4c_1\|\mathbf{E}\|_F}{\sqrt{d} - \sqrt{N-1}}, \end{aligned}$$

606 where the second inequality follows from  $\bar{\mathbf{U}}_X = \mathbf{V}^*$  and (33). Then, we complete the proof.

607  $\square$

608 **B Proofs in Section 3.2**

609 **B.1 Theoretical Justification of the DAE (15)**

610 Since  $\mathbf{x}_t = s_t \mathbf{x}_0 + \gamma_t \boldsymbol{\epsilon}$ , we compute

$$\mathbb{E}_\epsilon [\|\mathbf{U}_k^T (s_t \mathbf{x}_0 + \gamma_t \boldsymbol{\epsilon})\|^2] = s_t^2 \|\mathbf{U}_k^T \mathbf{x}_0\|^2 + \gamma_t^2 \mathbb{E}_\epsilon [\|\mathbf{U}_k^T \boldsymbol{\epsilon}\|^2] = s_t^2 \|\mathbf{U}_k^T \mathbf{x}_0\|^2 + \gamma_t^2 d,$$

611 where the first equality is due to  $\boldsymbol{\epsilon} \sim \mathcal{N}(\mathbf{0}, \mathbf{I}_n)$  and  $\mathbb{E}_\epsilon [\langle \mathbf{U}_k^T \mathbf{x}_0, \mathbf{U}_k^T \boldsymbol{\epsilon} \rangle] = \mathbf{0}$  for each  $k \in [K]$ . This  
612 implies that when  $n$  is sufficiently large, we can approximate  $w_k(\boldsymbol{\theta}; \mathbf{x}_t)$  in (8) well by

$$w_k(\boldsymbol{\theta}; \mathbf{x}_t) \approx \frac{\exp(\phi_t (s_t^2 \|\mathbf{U}_k^T \mathbf{x}_0\|^2 + \gamma_t^2 d))}{\sum_{l=1}^K \exp(\phi_t (s_t^2 \|\mathbf{U}_l^T \mathbf{x}_0\|^2 + \gamma_t^2 d))}.$$

613 This soft-max function can be further approximated by the hard-max function. Therefore, we di-  
614 rectly obtain (16).

615 **B.2 Proof of Theorem 3**

616 Equipped with the above setup, we are ready to prove Theorem 3.

617 *Proof of Theorem 3.* Plugging (15) into the integrand of (5) yields

$$\begin{aligned} & \mathbb{E}_\epsilon \left[ \left\| \frac{s_t}{s_t^2 + \gamma_t^2} \sum_{k=1}^K \hat{w}_k(\boldsymbol{\theta}; \mathbf{x}^{(i)}) \mathbf{U}_k \mathbf{U}_k^T (s_t \mathbf{x}^{(i)} + \gamma_t \boldsymbol{\epsilon}) - \mathbf{x}^{(i)} \right\|^2 \right] \\ &= \left\| \frac{s_t^2}{s_t^2 + \gamma_t^2} \sum_{k=1}^K \hat{w}_k(\boldsymbol{\theta}; \mathbf{x}^{(i)}) \mathbf{U}_k \mathbf{U}_k^T \mathbf{x}^{(i)} - \mathbf{x}^{(i)} \right\|^2 + \frac{(s_t \gamma_t)^2}{(s_t^2 + \gamma_t^2)^2} \mathbb{E}_\epsilon \left[ \left\| \sum_{k=1}^K \hat{w}_k(\boldsymbol{\theta}; \mathbf{x}^{(i)}) \mathbf{U}_k \mathbf{U}_k^T \boldsymbol{\epsilon} \right\|^2 \right] \\ &= \frac{s_t^2}{s_t^2 + \gamma_t^2} \sum_{k=1}^K \left( \frac{s_t^2}{s_t^2 + \gamma_t^2} \hat{w}_k^2(\boldsymbol{\theta}; \mathbf{x}^{(i)}) - 2\hat{w}_k(\boldsymbol{\theta}; \mathbf{x}^{(i)}) \right) \|\mathbf{U}_k^T \mathbf{x}^{(i)}\|^2 + \|\mathbf{x}^{(i)}\|^2 + \frac{(s_t \gamma_t)^2 d}{(s_t^2 + \gamma_t^2)^2} \sum_{k=1}^K \hat{w}_k(\boldsymbol{\theta}; \mathbf{x}^{(i)}), \end{aligned}$$

618 where the first equality follows from  $\mathbb{E}_\epsilon [\langle \mathbf{x}, \boldsymbol{\epsilon} \rangle] = 0$  for any fixed  $\mathbf{x} \in \mathbb{R}^n$  due to  $\boldsymbol{\epsilon} \sim \mathcal{N}(\mathbf{0}, \mathbf{I}_n)$ ,  
619 and the last equality uses  $\mathbf{U}_k \in \mathcal{O}^{n \times d}$  and  $\mathbf{U}_k^T \mathbf{U}_l = \mathbf{0}$  for all  $k \neq l$ . This, together with (5) and  
620  $\gamma_t = s_t \sigma_t$ , yields

$$\begin{aligned} \ell(\boldsymbol{\theta}) &= \frac{1}{N} \sum_{i=1}^N \sum_{k=1}^K \int_0^1 \frac{\lambda_t}{1 + \sigma_t^2} \left( \frac{1}{1 + \sigma_t^2} \hat{w}_k^2(\boldsymbol{\theta}; \mathbf{x}^{(i)}) - 2\hat{w}_k(\boldsymbol{\theta}; \mathbf{x}^{(i)}) \right) dt \|\mathbf{U}_k^T \mathbf{x}^{(i)}\|^2 + \\ & \frac{1}{N} \int_0^1 \lambda_t dt \sum_{i=1}^N \|\mathbf{x}^{(i)}\|^2 + \left( \int_0^1 \frac{\sigma_t^2 \lambda_t}{(1 + \sigma_t^2)^2} dt \right) \frac{d}{N} \sum_{i=1}^N \sum_{k=1}^K \hat{w}_k^2(\boldsymbol{\theta}; \mathbf{x}^{(i)}). \end{aligned}$$

621 According to (15), we can partition  $[N]$  into  $\{C_k(\boldsymbol{\theta})\}_{k=1}^K$ , where  $C_k(\boldsymbol{\theta})$  for each  $k \in [K]$  is defined  
622 as follows:

$$C_k(\boldsymbol{\theta}) := \left\{ i \in [N] : \|\mathbf{U}_k^T \mathbf{x}^{(i)}\| \geq \|\mathbf{U}_l^T \mathbf{x}^{(i)}\|, \forall l \neq k \right\}, \forall k \in [K]. \quad (34)$$

623 Then, we obtain

$$\sum_{i=1}^N \sum_{k=1}^K \hat{w}_k^2(\boldsymbol{\theta}; \mathbf{x}^{(i)}) = \sum_{k=1}^K \sum_{i \in C_k(\boldsymbol{\theta})} 1 = N.$$

624 This, together with plugging (34) into the above loss function, yields minimizing  $\ell(\boldsymbol{\theta})$  is equivalent  
625 to minimizing

$$\begin{aligned} & \frac{1}{N} \sum_{i=1}^N \sum_{k=1}^K \int_0^1 \frac{\lambda_t}{1 + \sigma_t^2} \left( \frac{1}{1 + \sigma_t^2} \hat{w}_k^2(\boldsymbol{\theta}; \mathbf{x}^{(i)}) - 2\hat{w}_k(\boldsymbol{\theta}; \mathbf{x}^{(i)}) \right) dt \|\mathbf{U}_k^T \mathbf{x}^{(i)}\|^2 \\ &= \left( \int_0^1 \frac{\lambda_t}{1 + \sigma_t^2} \left( \frac{1}{1 + \sigma_t^2} - 2 \right) dt \right) \frac{1}{N} \sum_{k=1}^K \sum_{i \in C_k(\boldsymbol{\theta})} \|\mathbf{U}_k^T \mathbf{x}^{(i)}\|^2. \end{aligned}$$

626 Since  $\frac{\lambda_t}{1+\sigma_t^2} \left( \frac{1}{1+\sigma_t^2} - 2 \right) < 0$  for all  $t \in [0, 1]$ , minimizing the above function is equivalent to

$$\max_{\boldsymbol{\theta}} \frac{1}{N} \sum_{k=1}^K \sum_{i \in C_k(\boldsymbol{\theta})} \|\mathbf{U}_k^T \mathbf{x}^{(i)}\|^2 \quad \text{s.t. } [\mathbf{U}_1 \dots \mathbf{U}_K] \in \mathcal{O}^{n \times dK}.$$

627 Then, we complete the proof. □

### 628 B.3 Proof of Theorem 4

629 *Proof of Theorem 4.* For ease of exposition, let  $\delta := \max\{\|\mathbf{e}_i\| : i \in [N]\}$ ,

$$f(\boldsymbol{\theta}) := \sum_{k=1}^K \sum_{i \in C_k(\boldsymbol{\theta})} \|\mathbf{U}_k^T \mathbf{x}^{(i)}\|^2,$$

630 and for each  $k \in [K]$ ,

$$C_k^* := \left\{ i \in [N] : \mathbf{x}^{(i)} = \mathbf{U}_k^* \mathbf{a}_i + \mathbf{e}_i \right\}.$$

631 Suppose that (51) and (52) hold with  $\mathbf{V} = \hat{\mathbf{U}}_k$  for all  $i \in [N]$  and  $k \neq l \in [K]$ , which happens with  
632 probability  $1 - 2K^2N^{-1}$  according to Lemma 5. This implies that for all  $i \in [N]$  and  $k \neq l \in [K]$ ,

$$\sqrt{d} - (2\sqrt{\log N} + 2) \leq \|\mathbf{a}_i\| \leq \sqrt{d} + (2\sqrt{\log N} + 2), \quad (35)$$

$$\|\hat{\mathbf{U}}_k^T \mathbf{U}_l^*\|_F - (2\sqrt{\log N} + 2) \leq \|\hat{\mathbf{U}}_k^T \mathbf{U}_l^* \mathbf{a}_i\| \leq \|\hat{\mathbf{U}}_k^T \mathbf{U}_l^*\|_F + (2\sqrt{\log N} + 2). \quad (36)$$

633 Recall that the underlying basis matrices are denoted by  $\boldsymbol{\theta}^* = \{\mathbf{U}_k^*\}_{k=1}^K$  and the optimal basis  
634 matrices are denoted by  $\hat{\boldsymbol{\theta}} = \{\hat{\mathbf{U}}_k\}_{k=1}^K$ .

635 First, we claim that  $C_k(\boldsymbol{\theta}^*) = C_k^*$  for each  $k \in [K]$ . Indeed, for each  $i \in C_k^*$ , we compute

$$\|\mathbf{U}_k^{*T} \mathbf{x}^{(i)}\| = \|\mathbf{U}_k^{*T} (\mathbf{U}_k^* \mathbf{a}_i + \mathbf{e}_i)\| = \|\mathbf{a}_i + \mathbf{U}_k^{*T} \mathbf{e}_i\| \geq \|\mathbf{a}_i\| - \|\mathbf{e}_i\|, \quad (37)$$

$$\|\mathbf{U}_l^{*T} \mathbf{x}^{(i)}\| = \|\mathbf{U}_l^{*T} (\mathbf{U}_k^* \mathbf{a}_i + \mathbf{e}_i)\| = \|\mathbf{U}_l^{*T} \mathbf{e}_i\| \leq \|\mathbf{e}_i\|, \quad \forall l \neq k. \quad (38)$$

636 This, together with (35) and  $\|\mathbf{e}_i\| < (\sqrt{d} - 2\sqrt{\log N})/2$ , implies  $\|\mathbf{U}_k^{*T} \mathbf{x}_i\| \geq \|\mathbf{U}_l^{*T} \mathbf{x}_i\|$  for all  $l \neq$   
637  $k$ . Therefore, we have  $i \in C_k(\boldsymbol{\theta}^*)$  due to (34). Therefore, we have  $C_k^* \subseteq C_k(\boldsymbol{\theta}^*)$  for each  $k \in [K]$ .  
638 This, together with the fact that they respectively denote a partition of  $[N]$ , yields  $C_k(\boldsymbol{\theta}^*) = C_k^*$  for  
639 each  $k \in [K]$ . Now, we compute

$$\begin{aligned} f(\boldsymbol{\theta}^*) &= \sum_{k=1}^K \sum_{i \in C_k^*} \|\mathbf{U}_k^{*T} \mathbf{x}^{(i)}\|^2 = \sum_{k=1}^K \sum_{i \in C_k^*} \|\mathbf{a}_i + \mathbf{U}_k^{*T} \mathbf{e}_i\|^2 \\ &= \sum_{i=1}^N \|\mathbf{a}_i\|^2 + 2 \sum_{k=1}^K \sum_{i \in C_k^*} \langle \mathbf{a}_i, \mathbf{U}_k^{*T} \mathbf{e}_i \rangle + \sum_{k=1}^K \sum_{i \in C_k^*} \|\mathbf{U}_k^{*T} \mathbf{e}_i\|^2. \end{aligned} \quad (39)$$

640 Next, we compute

$$\begin{aligned} f(\hat{\boldsymbol{\theta}}) &= \sum_{k=1}^K \sum_{i \in C_k(\hat{\boldsymbol{\theta}})} \|\hat{\mathbf{U}}_k^T \mathbf{x}^{(i)}\|^2 = \sum_{l=1}^K \sum_{k=1}^K \sum_{i \in C_k(\hat{\boldsymbol{\theta}}) \cap C_l^*} \|\hat{\mathbf{U}}_k^T (\mathbf{U}_l^* \mathbf{a}_i + \mathbf{e}_i)\|^2 \\ &= \sum_{l=1}^K \sum_{k=1}^K \sum_{i \in C_k(\hat{\boldsymbol{\theta}}) \cap C_l^*} \left( \|\hat{\mathbf{U}}_k^T \mathbf{U}_l^* \mathbf{a}_i\|^2 + 2 \langle \mathbf{a}_i, \mathbf{U}_l^{*T} \hat{\mathbf{U}}_k^T \mathbf{e}_i \rangle \right) + \sum_{k=1}^K \sum_{i \in C_k(\hat{\boldsymbol{\theta}})} \|\hat{\mathbf{U}}_k^T \mathbf{e}_i\|^2. \end{aligned}$$

641 This, together with  $f(\hat{\boldsymbol{\theta}}) \geq f(\boldsymbol{\theta}^*)$  and (39), yields

$$\begin{aligned}
\sum_{i=1}^N \|\mathbf{a}_i\|^2 - \sum_{l=1}^K \sum_{k=1}^K \sum_{i \in C_k(\hat{\boldsymbol{\theta}}) \cap C_l^*} \|\hat{\mathbf{U}}_k^T \mathbf{U}_l^* \mathbf{a}_i\|^2 &\leq \sum_{l=1}^K \sum_{k=1}^K \sum_{i \in C_k(\hat{\boldsymbol{\theta}}) \cap C_l^*} 2\langle \mathbf{a}_i, \mathbf{U}_l^{*T} \hat{\mathbf{U}}_k \hat{\mathbf{U}}_k^T \mathbf{e}_i \rangle + \\
&\sum_{k=1}^K \sum_{i \in C_k(\hat{\boldsymbol{\theta}})} \|\hat{\mathbf{U}}_k^T \mathbf{e}_i\|^2 - 2 \sum_{k=1}^K \sum_{i \in C_k^*} \langle \mathbf{a}_i, \mathbf{U}_k^{*T} \mathbf{e}_i \rangle - \sum_{k=1}^K \sum_{i \in C_k^*} \|\mathbf{U}_k^{*T} \mathbf{e}_i\|^2 \\
&\leq 4\delta \sum_{i=1}^N \|\mathbf{a}_i\| + N\delta^2 \leq 6\delta N\sqrt{d} + N\delta^2, \tag{40}
\end{aligned}$$

642 where the second inequality follows from  $\|\mathbf{e}_i\| \leq \delta$  for all  $i \in [N]$  and  $\mathbf{U}_k^*, \hat{\mathbf{U}}_k \in \mathcal{O}^{n \times d}$  for all  
643  $k \in [K]$ , and the last inequality uses (35).

644 For ease of exposition, let  $N_{kl} := |C_k(\hat{\boldsymbol{\theta}}) \cap C_l^*|$ . According to the pigeonhole principle, there exists  
645 a permutation  $\pi : [K] \rightarrow [K]$  such that there exists  $k \in [K]$  such that  $N_{\pi(k)k} \geq N/K^2$ . This,  
646 together with (40), yields

$$\begin{aligned}
6\delta N\sqrt{d} + N\delta^2 &\geq \sum_{i \in C_{\pi(k)}(\hat{\boldsymbol{\theta}}) \cap C_k^*} \left( \|\mathbf{a}_i\|^2 - \|\hat{\mathbf{U}}_{\pi(k)}^T \mathbf{U}_k^* \mathbf{a}_i\|^2 \right) \\
&= \langle \mathbf{I} - \mathbf{U}_k^{*T} \hat{\mathbf{U}}_{\pi(k)} \hat{\mathbf{U}}_{\pi(k)}^T \mathbf{U}_k^*, \sum_{i \in C_{\pi(k)}(\hat{\boldsymbol{\theta}}) \cap C_k^*} \mathbf{a}_i \mathbf{a}_i^T \rangle. \tag{41}
\end{aligned}$$

647 According to Lemma 6 and  $N_{\pi(k)k} \geq N/K^2$ , it holds with probability at least  $1 - 2K^4N^{-2}$  that

$$\left\| \frac{1}{N_{\pi(k)k}} \sum_{i \in C_{\pi(k)}(\hat{\boldsymbol{\theta}}) \cap C_k^*} \mathbf{a}_i \mathbf{a}_i^T - \mathbf{I} \right\| \leq \frac{9(\sqrt{d} + \sqrt{\log(N_{\pi(k)k})})}{\sqrt{N_{\pi(k)k}}}.$$

648 This, together with the Weyl's inequality, yields

$$\begin{aligned}
\lambda_{\min} \left( \sum_{i \in C_{\pi(k)}(\hat{\boldsymbol{\theta}}) \cap C_k^*} \mathbf{a}_i \mathbf{a}_i^T \right) &\geq N_{\pi(k)k} - 9\sqrt{N_{\pi(k)k}} \left( \sqrt{d} + \sqrt{\log(N_{\pi(k)k})} \right) \\
&\geq \frac{N}{K^2} - \frac{9\sqrt{N}}{K} \left( \sqrt{d} + \sqrt{\log N} \right) \geq \frac{N}{2K^2},
\end{aligned}$$

649 where the second inequality follows from  $N/K^2 \leq N_{\pi(k)k} \leq N$  and the last inequality is due to  
650  $\sqrt{N} \geq 18K(\sqrt{d} + \sqrt{\log N})$ . Using this and Lemma 7, we obtain

$$\begin{aligned}
&\langle \mathbf{I} - \mathbf{U}_k^{*T} \hat{\mathbf{U}}_{\pi(k)} \hat{\mathbf{U}}_{\pi(k)}^T \mathbf{U}_k^*, \sum_{i \in C_{\pi(k)}(\hat{\boldsymbol{\theta}}) \cap C_k^*} \mathbf{a}_i \mathbf{a}_i^T \rangle \\
&\geq \lambda_{\min} \left( \sum_{i \in C_{\pi(k)}(\hat{\boldsymbol{\theta}}) \cap C_k^*} \mathbf{a}_i \mathbf{a}_i^T \right) \text{Tr} \left( \mathbf{I} - \mathbf{U}_k^{*T} \hat{\mathbf{U}}_{\pi(k)} \hat{\mathbf{U}}_{\pi(k)}^T \mathbf{U}_k^* \right) \\
&\geq \frac{N}{2K^2} \text{Tr} \left( \mathbf{I} - \mathbf{U}_k^{*T} \hat{\mathbf{U}}_{\pi(k)} \hat{\mathbf{U}}_{\pi(k)}^T \mathbf{U}_k^* \right).
\end{aligned}$$

651 This, together with (41), implies

$$\text{Tr} \left( \mathbf{I} - \mathbf{U}_k^{*T} \hat{\mathbf{U}}_{\pi(k)} \hat{\mathbf{U}}_{\pi(k)}^T \mathbf{U}_k^* \right) \leq 2K^2 \left( 6\delta\sqrt{d} + \delta^2 \right).$$

652 Using this and  $[\mathbf{U}_1^*, \dots, \mathbf{U}_k^*] \in \mathcal{O}^{n \times dK}$ , we obtain

$$\begin{aligned}
\sum_{l \neq k} \|\hat{\mathbf{U}}_{\pi(k)}^T \mathbf{U}_l^*\|_F^2 &= \text{Tr} \left( \sum_{l \neq k} \hat{\mathbf{U}}_{\pi(k)}^T \mathbf{U}_l^* \mathbf{U}_l^{*T} \hat{\mathbf{U}}_{\pi(k)} \right) \leq \text{Tr} \left( \mathbf{I} - \hat{\mathbf{U}}_{\pi(k)}^T \mathbf{U}_k^* \mathbf{U}_k^{*T} \hat{\mathbf{U}}_{\pi(k)} \right) \\
&\leq 2K^2 \left( 6\delta\sqrt{d} + \delta^2 \right) \leq \frac{3d}{4}, \tag{42}
\end{aligned}$$

653 where the last inequality follows  $\delta \leq \sqrt{d}/(24K^2)$ . According to (40), we have

$$\begin{aligned} 6\delta N\sqrt{d} + N\delta^2 &\geq \sum_{l \neq k}^K \sum_{i \in C_{\pi(k)}(\hat{\theta}) \cap C_l^*} \left( \|\mathbf{a}_i\|^2 - \|\hat{\mathbf{U}}_{\pi(k)}^T \mathbf{U}_l^* \mathbf{a}_i\|^2 \right) \\ &\geq \sum_{l \neq k}^K N_{\pi(k)l} \left( (\sqrt{d} - \alpha)^2 - \left( \|\hat{\mathbf{U}}_{\pi(k)}^T \mathbf{U}_l^*\|_F + \alpha \right)^2 \right) \geq \frac{d}{8} \sum_{l \neq k}^K N_{\pi(k)l}, \end{aligned}$$

654 where the second inequality uses (35) and (36), and the last inequality follows from  $d \gtrsim \log N$ .  
655 Therefore, we have for each  $k \in [K]$ ,

$$\sum_{l \neq k}^K N_{\pi(k)l} \leq \frac{48\delta N\sqrt{d} + 8\delta^2 N}{d} < 1,$$

656 where the last inequality uses  $\delta \lesssim \sqrt{d/N}$ . This implies  $N_{\pi(l)k} = 0$  for all  $l \neq k$ , and thus  
657  $C_{\pi(k)}(\hat{\theta}) \subseteq C_k^*$ . Using the same argument, we can show that  $C_{\pi(l)}(\hat{\theta}) \subseteq C_l^*$  for each  $l \neq k$ .  
658 Therefore, we have  $C_{\pi(k)}(\hat{\theta}) = C_k^*$  for each  $k \in [K]$ . In particular, using the union bound yields  
659 event holds with probability at least  $1 - 2K^2N^{-1}$ . Based on the above optimal assignment, we can  
660 further show:

661 (i) Suppose that  $N_k \geq d$  for each  $k \in [K]$ . This, together with (i) in Theorem 2 and  $N_k \geq d$ , yields  
662 (18).

663 (ii) Suppose that there exists  $k \in [K]$  such that  $N_k < d$ . This, together with (ii) in Theorem 2 and  
664  $N_k \geq d$ , yields (19).

665 Finally, applying the union bound yields the probability of these events.  $\square$

## 666 C Experimental Setups in Section 2.2

667 In this section, we provide detailed setups for the experiments in Section 2.2. These experiments  
668 aim to validate the assumptions that real-world image data satisfies a mixture of low-rank Gaussians  
669 and that the DAE is parameterized according to (8). To begin, we show that  $\nabla_{\mathbf{x}_t} \mathbb{E}[\mathbf{x}_0 | \mathbf{x}_t]$  is of low  
670 rank when  $p_{\text{data}}$  follows a mixture of low-rank Gaussians and  $\sum_{k=1}^K d_k \leq n$ , where  $n$  is the ambient  
671 dimension of training samples.

### 672 C.1 Verification of Mixture of Low-Rank Gaussian Data Distribution

673 In this subsection, we demonstrate that a mixture of low-rank Gaussians is a reasonable and in-  
674 sightful model for approximating real-world image data distribution. To begin, we show that  
675  $\nabla_{\mathbf{x}_t} \mathbb{E}[\mathbf{x}_0 | \mathbf{x}_t]$  is of low rank when  $p_{\text{data}}$  follows a mixture of low-rank Gaussians with  $\sum_{k=1}^K d_k \leq n$ ,  
676 where  $n$  is the dimension of training samples.

677 **Lemma 2.** *Suppose that the data distribution  $p_{\text{data}}$  follows a mixture of low-rank Gaussian distri-  
678 butions as defined in Definition 1. For all  $t \in [0, 1]$ , it holds that*

$$\min_{k \in [K]} d_k \leq \text{rank}(\nabla_{\mathbf{x}_t} \mathbb{E}[\mathbf{x}_0 | \mathbf{x}_t]) \leq \sum_{k=1}^K d_k. \quad (43)$$

679 *Proof.* For ease of exposition, let

$$h_k(\mathbf{x}_t) := \exp(\phi_t \|\mathbf{U}_k^{*T} \mathbf{x}_t\|^2), \quad \forall k \in [K].$$

680 Obviously, we have

$$\nabla h_k(\mathbf{x}_t) := 2\phi_t \exp(\phi_t \|\mathbf{U}_k^{*T} \mathbf{x}_t\|^2) \mathbf{U}_k^* \mathbf{U}_k^{*T} \mathbf{x}_t = 2\phi_t h_k(\mathbf{x}_t) \mathbf{U}_k^* \mathbf{U}_k^{*T} \mathbf{x}_t. \quad (44)$$

681 According to Lemma 1, we have

$$\mathbb{E}[\mathbf{x}_0 | \mathbf{x}_t] = \frac{s_t}{s_t^2 + \gamma_t^2} f(\mathbf{x}_t), \quad \text{where } f(\mathbf{x}_t) := \frac{\sum_{k=1}^K \pi_k h_k(\mathbf{x}_t) \mathbf{U}_k^* \mathbf{U}_k^{*T} \mathbf{x}_t}{\sum_{k=1}^K \pi_k h_k(\mathbf{x}_t)}.$$

682 Then, we compute

$$\begin{aligned}
\nabla_{\mathbf{x}_t} f(\mathbf{x}_t) &= \frac{1}{\sum_{k=1}^K \pi_k h_k(\mathbf{x}_t)} \left( 2\phi_t \sum_{k=1}^K \pi_k h_k(\mathbf{x}_t) \mathbf{U}_k^* \mathbf{U}_k^{*T} \mathbf{x}_t \mathbf{x}_t^T \mathbf{U}_k^* \mathbf{U}_k^{*T} + \sum_{k=1}^K \pi_k h_k(\mathbf{x}_t) \mathbf{U}_k^* \mathbf{U}_k^{*T} \right) \\
&\quad - \frac{2\phi_t}{\left( \sum_{k=1}^K \pi_k h_k(\mathbf{x}_t) \right)^2} \left( \sum_{k=1}^K \pi_k h_k(\mathbf{x}_t) \mathbf{U}_k^* \mathbf{U}_k^{*T} \mathbf{x}_t \right) \left( \sum_{k=1}^K \pi_k h_k(\mathbf{x}_t) \mathbf{U}_k^* \mathbf{U}_k^{*T} \mathbf{x}_t \right)^T \\
&= \frac{1}{\sum_{k=1}^K \pi_k h_k(\mathbf{x}_t)} \sum_{k=1}^K \pi_k h_k(\mathbf{x}_t) (2\phi_t \mathbf{U}_k^* \mathbf{U}_k^{*T} \mathbf{x}_t \mathbf{x}_t^T + \mathbf{I}) \mathbf{U}_k^* \mathbf{U}_k^{*T} - \\
&\quad \frac{2\phi_t}{\left( \sum_{k=1}^K \pi_k h_k(\mathbf{x}_t) \right)^2} \left( \sum_{k=1}^K \pi_k h_k(\mathbf{x}_t) \mathbf{U}_k^* \mathbf{U}_k^{*T} \right) \mathbf{x}_t \mathbf{x}_t^T \left( \sum_{k=1}^K \pi_k h_k(\mathbf{x}_t) \mathbf{U}_k^* \mathbf{U}_k^{*T} \right).
\end{aligned}$$

683 This directly yields (43) for all  $t \in [0, 1]$ .  $\square$

684 Now, we conduct experiments to illustrate that diffusion models trained on real-world image datasets  
685 exhibit similar low-rank properties to those described in the above proposition. Provided that the  
686 DAE  $\mathbf{x}_\theta(\mathbf{x}_t, t)$  is applied to estimate  $\mathbb{E}[\mathbf{x}_0|\mathbf{x}_t]$ , we estimate the rank of the Jacobian of the DAE,  
687 i.e.,  $\nabla_{\mathbf{x}_t} \mathbf{x}_\theta(\mathbf{x}_t, t)$ , on the real-world data distribution, where  $\theta$  denotes the parameters of U-Net  
688 architecture trained on the real dataset. Also, this estimation is based on the findings in [55, 27] that  
689 under the training loss in Equation (5), the DAE  $\mathbf{x}_\theta(\mathbf{x}_t, t)$  converge to  $\mathbb{E}[\mathbf{x}_0|\mathbf{x}_t]$  as the number of  
690 training samples increases on the real data. We evaluate the numerical rank of the Jacobian of the  
691 DAE on four different datasets: CIFAR-10 [56], CelebA [57], FFHQ [58] and AFHQ [59], where  
692 the ambient dimension  $n = 3072$  for all datasets.

693 Given a random initial noise  $\mathbf{x}_1 \sim \mathcal{N}(\mathbf{0}, \mathbf{I}_n)$ , diffusion models generate a sequence of images  $\{\mathbf{x}_t\}$   
694 according to the reverse SDE in Eq. (3). Along the sampling trajectory  $\{\mathbf{x}_t\}$ , we calculate the  
695 Jacobian  $\nabla_{\mathbf{x}_t} \mathbf{x}_\theta(\mathbf{x}_t, t)$  and compute its numerical rank via

$$\text{rank}(\nabla_{\mathbf{x}_t} \mathbf{x}_\theta(\mathbf{x}_t, t)) := \arg \min \left\{ r \in [1, n] : \frac{\sum_{i=1}^r \sigma_i^2(\nabla_{\mathbf{x}_t} \mathbf{x}_\theta(\mathbf{x}_t, t))}{\sum_{i=1}^n \sigma_i^2(\nabla_{\mathbf{x}_t} \mathbf{x}_\theta(\mathbf{x}_t, t))} > \eta^2 \right\}. \quad (45)$$

696 In our experiments, we set  $\eta = 0.99$ . In the implementation, we utilize the Elucidating Diffusion  
697 Model (EDM) with the EDM noise scheduler [41] and DDPM++ architecture [51]. Moreover, we  
698 employ an 18-step Heun’s solver for sampling and present the results for 12 of these steps. For each  
699 dataset, we random sample 15 initial noise  $\mathbf{x}_1$ , calculate the mean of  $\text{rank}(\nabla_{\mathbf{x}_t} \mathbf{x}_\theta(\mathbf{x}_t, t))$  along  
700 the trajectory  $\{\mathbf{x}_t\}$ , and plot ratio of the numerical rank over the ambient dimension against the  
701 signal-noise-ratio (SNR)  $1/\sigma_t$  in Figure 2, where  $\sigma_t$  is defined in Eq. (2).

## 702 C.2 Verification of Low-Rank Network Parameterization

703 In this subsection, we empirically investigate the properties of U-Net architectures in diffusion mod-  
704 els and validate the simplification of the network architecture to Eq. (8). Based on the results in  
705 Appendix C.1, we use a mixture of low-rank Gaussian distributions for experiments. Here, we set  
706  $K = 2$ ,  $n = 48$ ,  $d_1 = d_2 = 6$ ,  $\pi_1 = \pi_2 = 0.5$ , and  $N = 1000$  for the data model Definition 1.  
707 Moreover, We use the EDM noise scheduler and 18-step Heun’s solver for both the U-Net and our  
708 proposed parameterization (8). To adapt the structure of the U-Net, we reshape each training sample  
709 into a 3D tensor with dimensions  $4 \times 4 \times 3$ , treating it as an image. Here, we use DDPM++ based  
710 diffusion models with a U-Net architecture. In each iteration, we randomly sampled a batch of im-  
711 age  $\{\mathbf{x}^{(j)}\}_{j=1}^{\text{bs}} \subseteq \{\mathbf{x}^{(i)}\}_{i=1}^N$ , along with a timestep  $t^{(j)}$  and a noise  $\epsilon^{(j)}$  for each image in the batch  
712 to optimize the training loss  $\ell(\theta)$ . We define

$$\text{kimgs} = \text{bs} \times \frac{\text{training iterations}}{1000} \quad (46)$$

713 to represent the total samples used for training. Here, we pick up the specific model trained under  
714 500 kimgs, 1000 kimgs, 2000 kimgs, and 6000 kimgs for evaluation, as shown in Figure 6(a).

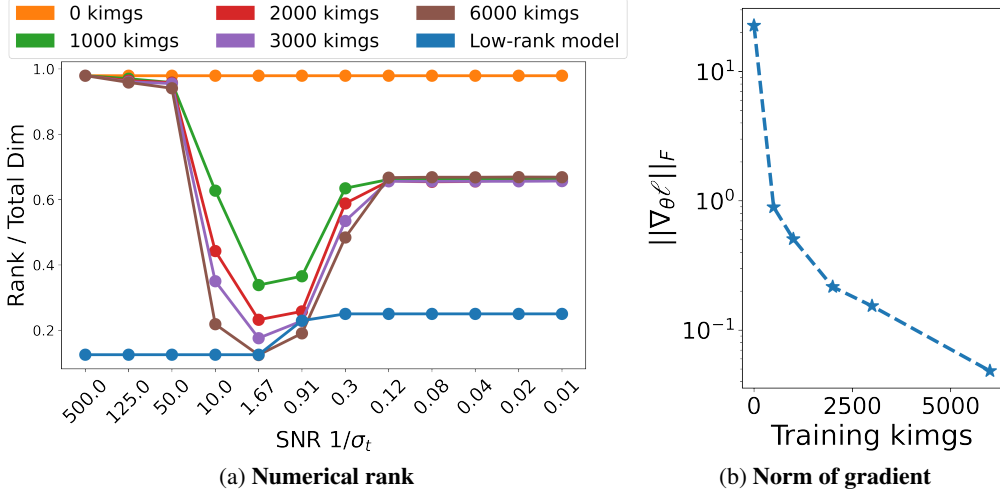


Figure 6: (a) **Numerical rank of  $\nabla_{\mathbf{x}_t} \mathbf{x}_\theta(\mathbf{x}_t, t)$  at all time of diffusion models.** Problem (5) is trained with the DAE  $\mathbf{x}_\theta(\cdot, t)$  parameterized according to (8) and U-Net on the training samples generated by the mixture of low-rank Gaussian distribution. The  $x$ -axis is the SNR and the  $y$ -axis is the numerical rank of  $\nabla_{\mathbf{x}_t} \mathbf{x}_\theta(\mathbf{x}_t, t)$  over the ambient dimension  $n$ , i.e.,  $\text{rank}(\nabla_{\mathbf{x}_t} \mathbf{x}_\theta(\mathbf{x}_t, t))/n$ . Here, *kings* denotes the number of samples used for training, which equals to training iterations times batch size of training samples. (b) **Convergence of gradient norm of the training loss:** The  $x$ -axis is kings (see Eq. (46)), and the  $y$ -axis is the gradient norm of the training loss.

---

**Algorithm 1** SGD for optimizing the training loss (5)

---

**Input:** Training samples  $\{\mathbf{x}^{(i)}\}_{i=1}^N$   
**for**  $j = 0, 1, 2, \dots, J$  **do**  
    Randomly select  $\{(i_m, t_m)\}_{m=1}^M$ , where  $i_m \in [N]$  and  $t_m \in (0, 1)$  and a noise  $\epsilon \sim \mathcal{N}(\mathbf{0}, \mathbf{I})$   
    Take a gradient step

$$\theta^{j+1} \leftarrow \theta^j - \frac{\eta}{M} \sum_{m \in [M]} \nabla_{\theta} \left\| \mathbf{x}_{\theta^j}(s_{t_m} \mathbf{x}^{(i_m)} + \gamma_{t_m} \epsilon, t_m) - \mathbf{x}^{(i_m)} \right\|^2$$

**end for**

---

715 We plot the numerical ranks of  $\nabla_{\mathbf{x}_t} \mathbf{x}_\theta(\mathbf{x}_t, t)$  for both our proposed parameterization in (8)  
716 and for the U-Net architecture in Figure 2(b). According to Lemma 2, it holds that  $6 \leq$   
717  $\text{rank}(\nabla_{\mathbf{x}_t} \mathbf{x}_\theta(\mathbf{x}_t, t)) \leq 12$ . This corresponds to the blue curve in Figure 2(b). To supplement  
718 our result in Figure 2(b), we further plot the numerical rank against SNR at different training iter-  
719 ations in Figure 6(a) and gradient norm of the objective against training iterations in Figure 6(b). We  
720 observe that with the training kings increases, the gradient for the U-Net  $\|\nabla_{\theta} \ell\|_F$  decrease smaller  
721 than  $10^{-1}$  and the rank ratio of  $\nabla_{\mathbf{x}_t} \mathbf{x}_\theta(\mathbf{x}_t, t)$  trained from U-Net gradually be close to the rank ratio  
722 from the low-rank model in the middle of the SNR ([0.91, 10.0]).

## 723 D Experimental Setups in Section 4

724 We use a CPU to optimize Problem (5) for the setting in Appendix D.1. For the settings in Ap-  
725 pendix D.2 and Appendix D.3, we employ a single A40 GPU with 48 GB memory to optimize  
726 Problem (5).

### 727 D.1 Learning the MoLRG distribution with the theoretical parameterization

728 Here, we present the stochastic gradient descent (SGD) algorithm for solving Problem (5) as follows:  
729

730 Now, we specify how to choose the parameters of the SGD in our implementation. We divide the  
 731 time interval  $[0, 1]$  into 64 time steps. When  $K = 1$ , we set the learning rate  $\eta = 10^{-4}$ , batch  
 732 size  $M = 128N_k$ , and number of iterations  $J = 10^4$ . When  $K = 2$ , we set the learning rate  
 733  $\eta = 2 \times 10^{-5}$ , batch size  $M = 1024$ , number of iterations  $J = 10^5$ . In particular, when  $K = 2$ , we  
 734 use the following tailor-designed initialization  $\boldsymbol{\theta}^0 = \{\mathbf{U}_k^0\}$  to improve the convergence of the SGD:

$$\mathbf{U}_k^0 = \mathbf{U}_k^* + 0.2\boldsymbol{\Delta}, \quad k \in \{1, 2\}, \quad (47)$$

735 where  $\boldsymbol{\Delta} \sim \mathcal{N}(\mathbf{0}, \mathbf{I}_n)$ . We calculate the success rate as follows. If the returned subspace basis  
 736 matrices  $\{\mathbf{U}_k\}_{k=1}^K$  satisfy

$$\frac{1}{K} \sum_{k=1}^K \|\mathbf{U}_{\Pi(k)} \mathbf{U}_{\Pi(k)}^T - \mathbf{U}_k^* \mathbf{U}_k^{*T}\| \leq 0.5$$

737 for some permutation  $\Pi : [K] \rightarrow [K]$ , it is considered successful.

## 738 D.2 Learning the MoLRG distribution with U-Net

739 we measure the generalization ability of U-Net via *generalization (GL) score* defined in Equa-  
 740 tion (48).

$$\text{GL score} = \frac{\mathcal{D}(\mathbf{x}_{\text{gen}}^{(i)})}{\mathcal{D}(\mathbf{x}_{\text{MoLRG}}^{(i)})}, \quad \mathcal{D}(\mathbf{x}^{(i)}) := \sum_{j=1}^N \min_{j \neq i} \|\mathbf{x}^{(i)} - \mathbf{x}^{(j)}\|, \quad (48)$$

741 where  $\{\mathbf{x}_{\text{MoLRG}}^{(i)}\}_{i=1}^N$  are samples generated from the MoLRG distribution and  $\{\mathbf{x}_{\text{gen}}^{(i)}\}_{i=1}^N$  are new sam-  
 742 ples generated by the trained U-Net. Intuitively,  $\mathcal{D}(\mathbf{x}_{\text{gen}}^{(i)})$  reflects the uniformity of samples in the  
 743 space: its value is small when the generated samples cluster around the training data, while the value  
 744 is large when generated samples disperse in the entire space. Therefore, the trained diffusion model  
 745 is in memorization regime when  $\mathcal{D}(\mathbf{x}_{\text{gen}}^{(i)}) \ll \mathcal{D}(\mathbf{x}_{\text{MoLRG}}^{(i)})$  and the GL score is close to 0, while it is in  
 746 generalization regime when  $\mathcal{D}(\mathbf{x}_{\text{gen}}^{(i)}) \approx \mathcal{D}(\mathbf{x}_{\text{MoLRG}}^{(i)})$  and the GL score is close to 1.

747 In our implementation, we set the total dimension of MoLRG as  $n = 48$  and the number of training  
 748 samples  $N_{\text{eval}} = 1000$ . To train the U-Net, we use the stochastic gradient descent in Algorithm 1.  
 749 We use DDPM++ architecture [11] for the U-Net and EDM [41] noise scheduler. We set the learning  
 750 rate  $10^{-3}$ , batch size 64, and number of iterations  $J = 10^4$ .

## 751 D.3 Learning real-world image data distributions with U-Net

752 According to [27], we define the generalization (GL) score on real-world image dataset as follows:

$$\text{GL score} := 1 - \mathbb{P} \left( \max_{i \in [N]} [\mathcal{M}_{\text{SSCD}}(\mathbf{x}, \mathbf{y}_i)] > 0.6 \right). \quad (49)$$

753 Here, the SSCD similarity is first introduced in [60] to measure the replication between image pair  
 754  $(\mathbf{x}_1, \mathbf{x}_2)$ , which is defined as follows:

$$\mathcal{M}_{\text{SSCD}}(\mathbf{x}_1, \mathbf{x}_2) = \frac{\text{SSCD}(\mathbf{x}_1) \cdot \text{SSCD}(\mathbf{x}_2)}{\|\text{SSCD}(\mathbf{x}_1)\|_2 \cdot \|\text{SSCD}(\mathbf{x}_2)\|_2}$$

755 where  $\text{SSCD}(\cdot)$  represents a neural descriptor for copy detection of images. We empirically sam-  
 756 ple 10K initial noises to estimate the probability. Intuitively, GL score measures the dissimilarity  
 757 between the generated sample  $\mathbf{x}$  and all  $N$  samples  $\mathbf{y}_i$  from the training dataset  $\{\mathbf{y}_i\}_{i=1}^N$ .

758 To train diffusion models for real-world image datasets, we use the DDPM++ architecture [11] for  
 759 the U-Net and variance preserving (VP) [11] noise scheduler. The U-Net is trained using the Adam  
 760 optimizer [61], a variant of SGD in Algorithm 1. We set the learning rate  $\eta = 10^{-3}$ , batch size  
 761  $M = 512$ , and the total number of iterations  $10^5$ .

## 762 D.4 Correspondence between low-dimensional subspaces and image semantics

763 We denote the Jacobian of the DAE  $\mathbf{x}_\theta(\mathbf{x}_t, t)$  by  $\mathbf{J}_t := \nabla_{\mathbf{x}_t} \mathbf{x}_\theta(\mathbf{x}_t, t) \in \mathbb{R}^{n \times n}$  and let  $\mathbf{J}_t = \mathbf{U} \boldsymbol{\Sigma} \mathbf{V}^T$   
 764 be an singular value decomposition (SVD) of  $\mathbf{J}_t$ , where  $r = \text{rank}(\mathbf{J}_t)$ ,  $\mathbf{U} = [\mathbf{u}_1, \dots, \mathbf{u}_r] \in \mathcal{O}^{n \times r}$ ,

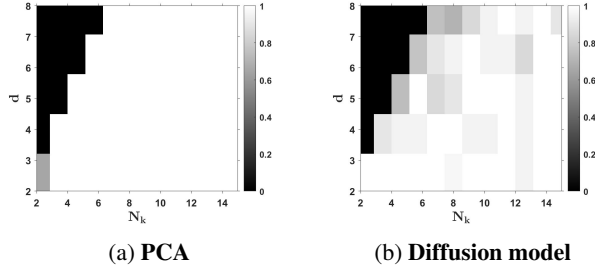


Figure 7: **Phase transition of learning the MoLRG distribution when  $K = 3$ .** The  $x$ -axis is the number of training samples and  $y$ -axis is the dimension of subspaces. We apply a subspace clustering method and train diffusion models for solving Problems (17) and (5), visualizing the results in (a) and (b), respectively.

765  $\mathbf{V} = [\mathbf{v}_1, \dots, \mathbf{v}_r] \in \mathcal{O}^{n \times r}$ , and  $\mathbf{\Sigma} = \text{diag}(\sigma_1, \dots, \sigma_r)$  with  $\sigma_1 \geq \dots \geq \sigma_r$  being the singular  
 766 values. According to the results in Figure 2, it is observed that  $\mathbf{J}_t$  is low rank, i.e.,  $r \ll n$ . Now, we  
 767 compute the first-order approximation of  $\mathbf{x}_\theta(\mathbf{x}_t, t)$  along the direction of  $\mathbf{v}_i \in \mathbb{R}^n$ , where  $\mathbf{v}_i$  is the  
 768  $i$ -th right singular vector of  $\mathbf{J}_t$ :

$$\mathbf{x}_\theta(\mathbf{x}_t + \alpha \mathbf{v}_i, t) \approx \mathbf{x}_\theta(\mathbf{x}_t, t) + \alpha \mathbf{J}_t \mathbf{v}_i = \mathbf{x}_\theta(\mathbf{x}_t, t) + \alpha \sigma_i \mathbf{u}_i,$$

769 where the last equality follows from  $\mathbf{J}_t \mathbf{v}_i = \mathbf{U} \mathbf{\Sigma} \mathbf{V}^T \mathbf{v}_i = \alpha \sigma_i \mathbf{u}_i$ . To validate the semantic meaning  
 770 of the basis  $\mathbf{v}_i$ , we vary the value of  $\alpha$  from negative to positive and visualize the resulting changes  
 771 in the generated images. Figures 5, 8 and 9(a, c) illustrate some real examples.

772 In the experiments, we use a pre-trained diffusion denoising probabilistic model (DDPM) [2] on the  
 773 MetFaces dataset [50]. We randomly select an image  $\mathbf{x}_0$  from this dataset and use the reverse process  
 774 of the diffusion denoising implicit model (DDIM) [51] to generate  $\mathbf{x}_t$  at  $t = 0.7T$  (ablation studies  
 775 for  $t = 0.1T$  and  $0.9T$  are shown in Figure 9(b)), where  $T$  denote the total number of time steps.  
 776 We respectively choose the changed direction as the leading right singular vectors  $\mathbf{v}_1, \mathbf{v}_3, \mathbf{v}_4, \mathbf{v}_5, \mathbf{v}_6$   
 777 and use  $\tilde{\mathbf{x}}_t = \mathbf{x}_t + \alpha \mathbf{v}_i$  to generate new images with  $\alpha \in [-6, 6]$  shown in Figures 5, 8 and 9(a, c).

## 778 E Auxiliary Results

779 First, we present a probabilistic result to prove Theorem 2, which provides an optimal estimate of  
 780 the small singular values of a matrix with i.i.d. Gaussian entries. This lemma is proved in [62,  
 781 Theorem 1.1].

782 **Lemma 3.** *Let  $\mathbf{A}$  be an  $m \times n$  random matrix, where  $m \geq n$ , whose elements are independent*  
 783 *copies of a subgaussian random variable with mean zero and unit variance. It holds for every  $\varepsilon > 0$*   
 784 *that*

$$\mathbb{P}(\sigma_{\min}(\mathbf{A}) \geq \varepsilon(\sqrt{m} - \sqrt{n-1})) \geq 1 - (c_1 \varepsilon)^{m-n+1} - \exp(-c_2 m),$$

785 where  $c_1, c_2 > 0$  are constants depending polynomially only on the subgaussian moment.

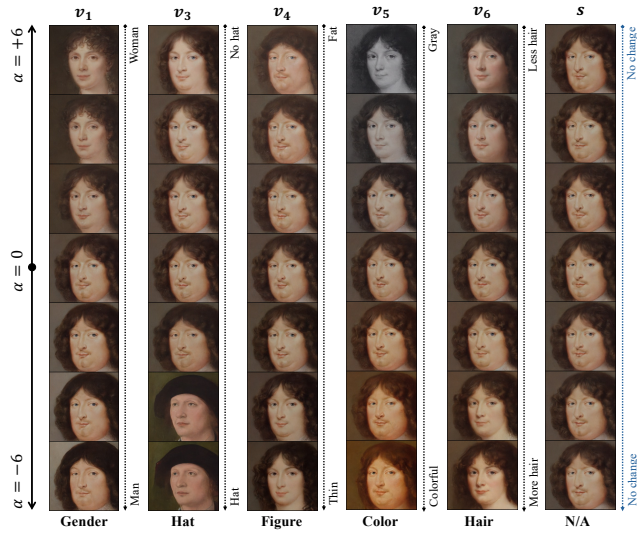
786 Next, we present a probabilistic bound on the deviation of the norm of weighted sum of squared  
 787 Gaussian random variables from its mean. This is a direct extension of [63, Theorem 5.2.2].

788 **Lemma 4.** *Let  $\mathbf{x} \sim \mathcal{N}(\mathbf{0}, \mathbf{I}_d)$  be a Gaussian random vector and  $\lambda_1, \dots, \lambda_d > 0$  be constants. It*  
 789 *holds for any  $t > 0$  that*

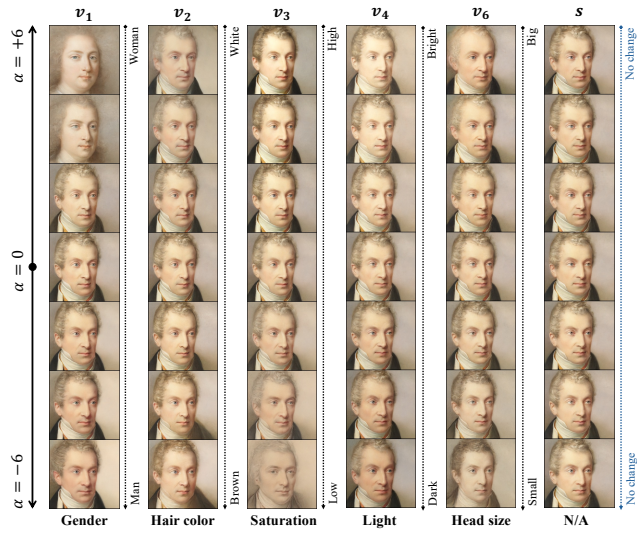
$$\mathbb{P}\left(\left|\sqrt{\sum_{i=1}^d \lambda_i^2 x_i^2} - \sqrt{\sum_{i=1}^d \lambda_i^2}\right| \geq t + 2\lambda_{\max}\right) \leq 2 \exp\left(-\frac{t^2}{2\lambda_{\max}^2}\right), \quad (50)$$

790 where  $\lambda_{\max} = \max\{\lambda_i : i \in [d]\}$ .

791 Based on the above lemma, we can further show the following concentration inequalities to estimate  
 792 the norm of the standard norm Gaussian random vector.



(a)



(b)

Figure 8: Correspondence between the singular vectors of the Jacobian of the DAE and semantic image attributes.



Figure 9: Correspondence between the singular vectors of the Jacobian of the DAE and semantic image attributes. (a,c) Additional examples when  $t = 0.7T$ . (b) Ablation studies when  $t = 0.1T$  and  $0.9T$ .

793 **Lemma 5.** Suppose that  $\mathbf{a}_i \stackrel{i.i.d.}{\sim} \mathcal{N}(\mathbf{0}, \mathbf{I}_d)$  is a Gaussian random vector for each  $i \in [N]$ . The  
 794 following statements hold:

795 (i) It holds for all  $i \in [N]$  with probability at least  $1 - N^{-1}$  that

$$\left| \|\mathbf{a}_i\| - \sqrt{d} \right| \leq 2\sqrt{\log N} + 2. \quad (51)$$

796 (ii) Let  $\mathbf{V} \in \mathcal{O}^{n \times d}$  be given. For all  $i \in C_k^*$  and all  $k \in [K]$ , it holds with probability at least  
 797  $1 - 2N^{-1}$  that

$$\left| \|\mathbf{V}^T \mathbf{U}_k^* \mathbf{a}_i\| - \|\mathbf{V}^T \mathbf{U}_k^*\|_F \right| \leq 2\sqrt{\log N} + 2. \quad (52)$$

798 *Proof.* (i) Applying Lemma 4 to  $\mathbf{a}_i \sim \mathcal{N}(\mathbf{0}, \mathbf{I}_d)$ , together with setting  $t = 2\sqrt{\log N}$  and  $\lambda_j = 1$  for  
 799 all  $j \in [d]$ , yields

$$\mathbb{P} \left( \left| \|\mathbf{a}_i\| - \sqrt{d} \right| \geq 2\sqrt{\log N} + 2 \right) \leq 2N^{-2}.$$

800 This, together with the union bound, yields that (51) holds with probability  $1 - N^{-1}$ .

801 (ii) Let  $\mathbf{V}^T \mathbf{U}_k^* = \mathbf{P} \mathbf{\Sigma} \mathbf{Q}^T$  be a singular value decomposition of  $\mathbf{V}^T \mathbf{U}_k^*$ , where  $\mathbf{\Sigma} \in \mathbb{R}^{d \times d}$  with the  
 802 diagonal elements  $0 \leq \sigma_d \leq \dots \leq \sigma_1 \leq 1$  being the singular values of  $\mathbf{V}^T \mathbf{U}_k^*$  and  $\mathbf{P}, \mathbf{Q} \in \mathcal{O}^d$ . This,  
 803 together with the orthogonal invariance of the Gaussian distribution, yields

$$\|\mathbf{V}^T \mathbf{U}_k^* \mathbf{a}_i\| = \|\mathbf{\Sigma} \mathbf{Q}^T \mathbf{a}_i\| \stackrel{d}{=} \|\mathbf{\Sigma} \mathbf{a}_i\| = \sqrt{\sum_{j=1}^d \sigma_j^2 a_{ij}^2}. \quad (53)$$

804 Using Lemma 4 with setting  $t = 2\sigma_1 \sqrt{\log N}$  and  $\lambda_j = \sigma_j \leq 1$  for all  $j$  yields

$$\mathbb{P} \left( \left| \|\mathbf{V}^T \mathbf{U}_k^* \mathbf{a}_i\| - \|\mathbf{V}^T \mathbf{U}_k^*\|_F \right| \geq \sigma_1 \alpha \right) = \mathbb{P} \left( \left| \sqrt{\sum_{j=1}^d \sigma_j^2 a_{ij}^2} - \sqrt{\sum_{j=1}^d \sigma_j^2} \right| \geq \sigma_1 \alpha \right) \leq 2N^{-2}.$$

805 This, together with  $\sigma_1 \leq 1$  and the union bound, yields (52).  $\square$

806 Next, We present a spectral bound on the covariance estimation for the random vectors generated by  
 807 the normal distribution.

808 **Lemma 6.** Suppose that  $\mathbf{a}_1, \dots, \mathbf{a}_N \in \mathbb{R}^d$  are i.i.d. standard normal random vectors, i.e.,  $\mathbf{a}_i \stackrel{i.i.d.}{\sim}$   
 809  $\mathcal{N}(\mathbf{0}, \mathbf{I}_d)$  for all  $i \in [N]$ . Then, it holds with probability at least  $1 - 2N^{-2}$  that

$$\left\| \frac{1}{N} \sum_{i=1}^N \mathbf{a}_i \mathbf{a}_i^T - \mathbf{I}_d \right\| \leq \frac{9(\sqrt{d} + \sqrt{\log N})}{\sqrt{N}}, \quad (54)$$

810 *Proof.* According to [63, Theorem 4.7.1], it holds that

$$\mathbb{P} \left( \left\| \frac{1}{N} \sum_{i=1}^N \mathbf{a}_i \mathbf{a}_i^T - \mathbf{I}_d \right\| \geq \frac{9(\sqrt{d} + \eta)}{\sqrt{N}} \right) \leq 2 \exp(-2\eta^2),$$

811 where  $\eta > 0$ . Plugging  $\eta = \sqrt{\log N}$  into the above inequality yields

$$\mathbb{P} \left( \left\| \frac{1}{N} \sum_{i=1}^N \mathbf{a}_i \mathbf{a}_i^T - \mathbf{I}_d \right\| \geq \frac{9(\sqrt{d} + \sqrt{\log N})}{\sqrt{N}} \right) \leq 2N^{-2}.$$

812 This directly implies (54).  $\square$

813 **Lemma 7.** Let  $\mathbf{A}, \mathbf{B} \in \mathbb{R}^{n \times n}$  be positive semi-definite matrices. Then, it holds that

$$\langle \mathbf{A}, \mathbf{B} \rangle \geq \lambda_{\min}(\mathbf{A}) \text{Tr}(\mathbf{B}). \quad (55)$$

814 *Proof.* Let  $\mathbf{U} \mathbf{\Lambda} \mathbf{U}^T = \mathbf{A}$  be an eigenvalue decomposition of  $\mathbf{A}$ , where  $\mathbf{U} \in \mathcal{O}^n$  and  $\mathbf{\Sigma} =$   
 815  $\text{diag}(\lambda_1, \dots, \lambda_n)$  is a diagonal matrix with diagonal entries  $\lambda_1 \geq \dots \geq \lambda_n \geq 0$  being the eigenval-  
 816 ues. Then, we compute

$$\langle \mathbf{A}, \mathbf{B} \rangle = \langle \mathbf{U} \mathbf{\Lambda} \mathbf{U}^T, \mathbf{B} \rangle = \langle \mathbf{\Lambda}, \mathbf{U} \mathbf{B} \mathbf{U}^T \rangle \geq \lambda_{\min}(\mathbf{A}) \text{Tr}(\mathbf{U} \mathbf{B} \mathbf{U}^T) = \lambda_{\min}(\mathbf{A}) \text{Tr}(\mathbf{B}),$$

817 where the inequality follows from  $\lambda_i \geq 0$  for all  $i \in [N]$  and  $\mathbf{B}$  is a positive semidefinite matrix.  $\square$